This is the preprint version of the following article:
Tian Lu and Qinxue Chen, Visualization Analysis of Weak Interactions in Chemical Systems. In Comprehensive Computational Chemistry, vol. 2, pp. 240-264. Oxford: Elsevier (2024)
http://dx.doi.org/10.1016/B978-0-12-821978-2.00076-3

Visualization Analysis of Weak Interactions in Chemical Systems

Tian Lu* and Qinxue Chen

Beijing Kein Research Center for Natural Sciences, 11-1-301, Nanli 4th Yard, Sanjianfang, Chaoyang District, Beijing 100024, P. R. China

* Correspondence author. E-mail: sobereva@sina.com

Author information

Tian Lu ORCiD: 0000-0002-1822-1229 E-mail: sobereva@sina.com

Qinxue Chen: ORCiD: 0000-0003-0155-2387 E-mail: qinxue_chen@sina.com

Abstract

The visual analysis techniques of weak interactions in chemical systems represented by non-covalent interaction (NCI) method have become increasingly popular in the past 10 years. These methods allow chemists to conveniently and intuitively understand what kinds of interactions exist in which areas, and to a certain extent the interaction strengths can also be analyzed quantitatively. This chapter presents a comprehensive and systematic introduction to NCI and various subsequent analysis methods that closely related to it. Readers will learn about the idea, principle, characteristics, and application scope of different methods. At the same time, this chapter will briefly introduce the Multiwfn program that can realize these analyses.

Objectives box

After reading this chapter, the readers will understand the following information:

1. Theoretical background of various visualization analysis methods
2. What problems can be studied by the analysis methods

3. Pros and cons of different methods
4. Program implementation of the introduced methods

Keywords: Chemical bond; hydrogen bond; interaction region indicator; independent gradient model; molecular complex; Multiwfn; non-covalent interaction; pi-pi stacking; visual analysis; van der Waals interaction; weak interaction; wavefunction analysis; quantum chemistry; electron density

1. Introduction

Weak interactions are ubiquitous in wide variety of chemical systems and have many specific forms, such as hydrogen-bond (H-bond),[1, 2] halogen-bond (X-bond),[3-6] chalcogen bond,[7] pnicogen-bond,[8, 9] dihydrogen bond,[10] van der Waals (vdW) interaction,[11] π-π stacking,[12, 13] and steric hindrance.[14] They have key influence on properties of condensed phase and a large number of problems in chemistry field, including molecular recognition, supramolecular self-assembly, ligand-receptor binding, molecular preferential conformation, and so on. Currently, weak interaction is one of the hottest research topics in theoretical and computational chemistry, while in the field of crystal engineering and drug design, it is a crucial factor that must always be carefully considered.

Traditionally, weak interactions are mainly studied by binding energy and geometry parameters at optimized structure, and sometimes they are further characterized by additional techniques such as atom-in-molecules (AIM) theory,[15-18] NBO second order perturbation theory,[19, 20] and energy decomposition analysis.[21, 22] While in the last decade, visual analysis methods of weak interactions have been developed vigorously and attracted increasing attention. This kind of method is able to represent weak interactions in chemical systems in a very intuitive and physically meaningful manner, so that researchers can easily understand their main occurrence region, characteristics and nature. Due to the important practical value and great convenience, these methods have been employed in a large number of publications and have even become indispensable means in weak interaction studies. It is particularly worth mentioning that the article introducing the visual analysis method named non-covalent interaction (NCI)[23] has been cited as many as 4000 times since its publication in 2010, which sufficiently renders its great popularity. We believe it is of great value to present a systematic overview of the NCI and all subsequent developments, which will enable readers to comprehensively recognize the principle, characteristics, relationship and practical significance of the methods, so that they can easily choose the most appropriate one to study their own actual problems to gain a deeper insight.

This is exactly the purpose of this chapter.

The following content of this chapter is organized as follows. In Section 2, we will carefully introduce NCI method, whose basic idea and application examples will be given, its relationship with AIM will be discussed, and some notes on practical use will be mentioned. From Section 3 to Section 7, other methods that closely related to NCI will be described and compared with NCI. Section 8 will briefly introduce the powerful Multiwfn program[24] that can realize almost all these visual analysis methods, and meantime a simple example of performing NCI analysis will be presented. All plane maps and isosurface maps in this chapter were directly plotted by Multiwfn 3.8, or rendered by VMD 1.9.3[25] based on files exported by Multiwfn.

2. NCI method

The NCI method proposed by Yang and coworkers is a very popular way to graphically display the areas and types of weak interactions in a chemical system. Due to its universality and convenience, it has been prevalently employed by chemists in theoretical study of weak interactions for a wide variety of systems, such as intramolecular hydrogen-bond,[26, 27] π-π stacking,[12] interaction of metal cation with atomic cluster,[28] ligand-protein binding,[29] interactions in molecular crystal,[24] and so on. The NCI method will be comprehensively introduced in this section. Due to the great success of the NCI method, some researchers later proposed different methods closely related to it to further extend its application scope, or provide complementary information, which will be introduced in the later sections in this chapter.

2.1 Idea of NCI analysis

The central idea of NCI method is using isosurfaces of a three-dimensional scalar function named reduced density gradient function (RDG) to reveal the regions where weak interaction mainly occurs. The RDG corresponds to dimensionless form of magnitude of electron density gradient and is defined as

$$\mathrm{RDG}(\mathbf{r}) = \frac{1}{2(3\pi^2)^{1/3}} \frac{|\nabla\rho(\mathbf{r})|}{\rho(\mathbf{r})^{4/3}} \tag{1}$$

where ρ is electron density, which is usually generated by quantum chemistry calculation, but may also be determined by high-resolution crystal diffraction. The characters of ρ, its gradient norm $|\nabla\rho|$ and RDG in different regions of common chemical systems are listed in Table 1, As can be seen, RDG is relatively small in both chemical bond and weak interaction regions, while the ρ around chemical bond regions is evidently larger than that around weak interaction regions. So, if only the regions with low electron density are taken into account, the RDG isosurfaces with a small isovalue will be able to display the regions where weak interactions occur. In NCI analysis, RDG isosurface with an isovalue of 0.4 to 0.6 is often used to graphically exhibit weak interactions, and in the region where ρ is larger than a threshold, the RDG is set to an arbitrary large value to suppress occurrence of its isosurfaces. The threshold is usually chosen to be 0.05 a.u., since ρ in weak interaction regions is rarely higher than this value. However, the weak interactions with partial covalency, such as charged H-bonds,[1] could have evidently larger ρ in the interaction region, and the threshold thus needs to be adjusted appropriately according to the actual situation.

Table 1 Character of electron density, magnitude of electron density and RDG function in different regions

	Around nuclei	Around chemical bonds	Weak interaction regions	Boundary of molecule
$\lvert\nabla\rho(\mathbf{r})\rvert$	Large	0~Minor	0 ~ Small	Very small ~ Small
$\rho(\mathbf{r})$	Large	Medium	Small	0~Small
RDG($\mathbf{r}$)	Medium	0~Minor	0 ~ Medium	Medium ~Very large

Let us examine distribution of RDG for a typical weakly interacting system, $HCCH\cdots NH_3$ H-bond complex. From the RDG plane map in Fig. 1(a) it can be seen that RDG is indeed small in the H-bond region. The RDG = 0.5 isosurface map is shown in Fig. 1(b), in which the isosurfaces not only occur in weak interaction region, but also visible around chemical bonds. The difference between Fig. 1(c) and Fig. 1(b) is that in the former, the RDG isosurfaces are fully shielded in the regions where ρ is larger than 0.05 a.u. It can be seen from Fig. 1(c) that the RDG isosurface nicely reveals the H-bond, and meantime no isosurface occurs in undesirable areas. This example demonstrates that employing RDG with a properly selected truncation value of ρ is a reasonable way of visually revealing weak interactions.

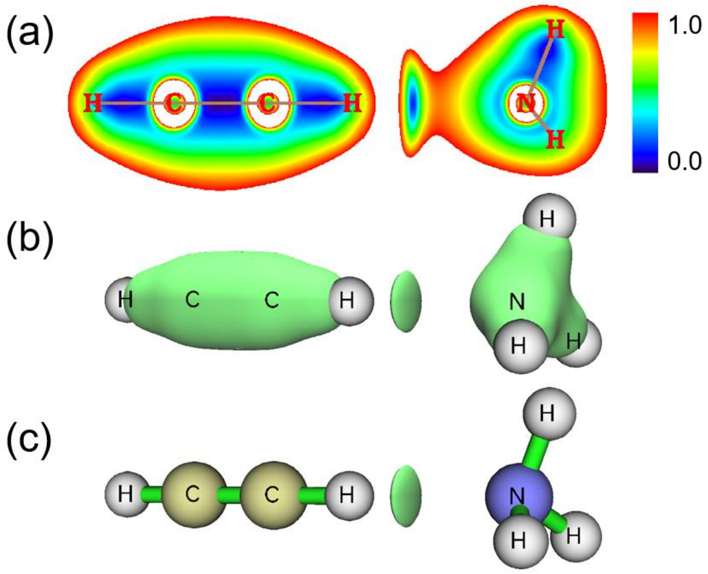

Fig. 1 RDG map of HCCH···NH_3 complex. (a) Color-filled plane map. The region with RDG larger than 1.0 is shown as white (b) Isosurface of RDG = 0.5 (c) Isosurface of RDG = 0.5 with shielding of isosurfaces in the regions where electron density is larger than 0.05 a.u.

In addition, NCI method also proposes to map $sign(\lambda_2)\rho$ function on the RDG isosurfaces via different colors to visually distinguish the type of interactions. $sign(\lambda_2)\rho$ denotes product of ρ and sign of λ_2, where the λ_2 stands for the second largest Hessian matrix of ρ. The idea of the definition of the $sign(\lambda_2)\rho$ is not difficult to comprehend. In the Bader's famous AIM theory,[16, 17] critical point (CP) refers to the position where magnitude of gradient of ρ is zero. The so-called (3,-1) type of CP commonly appears between two attractive atoms and hence is referred to as bond critical point (BCP). The (3,+1) type of CP often implies that electron is locally depleted at this position and exhibits steric effect, it generally occurs at the center of a ring. The standard for distinguishing (3,-1) and (3,+1) types of CPs is the sign of λ_2. If λ_2 at a CP is larger than zero, then the CP type is (3,+1), else (3,-1). Besides, strength of weak interactions is known to have approximately positive correlation with ρ in the interaction region. Due to the above characteristics of λ_2 and ρ, it is naturally expected that $sign(\lambda_2)\rho$ should have a certain ability to characterize type of weak interactions. The commonly used color scale for mapping $sign(\lambda_2)\rho$ on RDG isosurfaces is given as Fig. 2, the interpretation of different ranges of color is also marked. Note that due to the complexity and variety of interactions in chemical systems, the annotations in this figure are only suitable for general situations. Readers should correctly recognize the essential meaning of the colors according to the definition of $sign(\lambda_2)\rho$.

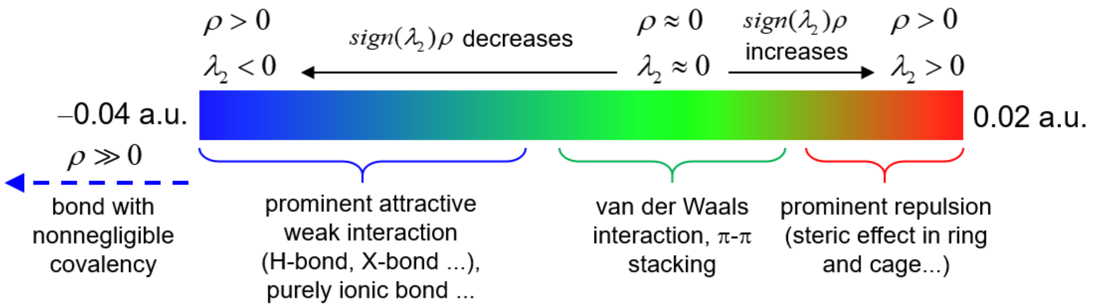

Fig. 2 Commonly used color scale in NCI map and common interpretation of various color ranges.

vdW interaction region always has a very small ρ, so the corresponding color of $sign(\lambda_2)\rho$ in Fig. 2 is green. π-π stacking has the same physical nature as the attractive part of vdW interaction, that is, dispersion effect,[13] therefore the ρ in π-π stacking region is also quite small. The regions corresponding to evident steric effect or attractive weak interactions (for example, the H-bond and X-bond of medium strength) have a relatively large ρ (typically 0.02 ~ 0.05 a.u.), so they correspond to blue and red zones in Fig. 2, respectively. It is noteworthy that although the strength of ionic bonds is usually one order of magnitude larger than that of weak interactions, the magnitude of ρ in their interaction regions is comparable. For example, the ρ at BCP of Na-Cl bond is merely about 0.03 a.u. So, RDG isosurfaces can not only reveal weak interactions, but also exhibit ionic bond interactions. In contrast, the interactions with nonnegligible covalency, especially covalent bonds, usually have ρ in the interaction region significantly larger than 0.05 a.u., therefore they are not visible in the standard NCI map, which considers density truncation. Clearly, NCI essentially is a method focusing on revealing various non-covalent interactions.

2.2 Examples of NCI analysis

The NCI map for phenol dimer, which is a representative weak interaction complex, is given in Fig. 3(a). The isosurfaces correspond to RDG of 0.5, and $sign(\lambda_2)\rho$ is mapped on them according to the color bar in Fig. 2. It can be seen that the NCI map vividly exhibits various featured interaction regions. The light blue oblate isosurface reveals the H-bond, the two slender red isosurfaces represent the notable steric effect in the six-membered rings, the wide green isosurface shows the intermolecular vdW interaction. It is evident that this NCI map successfully reveals all kinds of weak interaction in the phenol dimer.

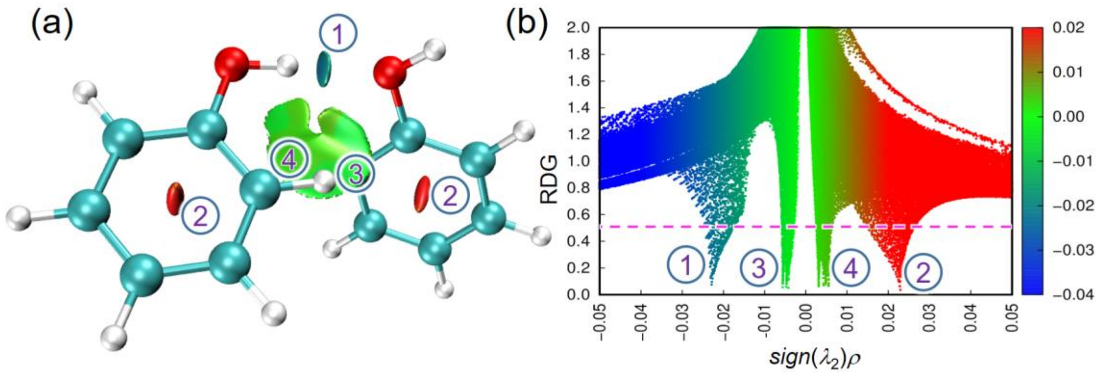

Fig. 3 (a) NCI map of phenol dimer. Isosurfaces of RDG = 0.5 are colored by $sign(\lambda_2)\rho$ according to the color bar of Fig. 2. (b) Scatter map between RDG and $sign(\lambda_2)\rho$ of the grid points used to plot (a). Correspondence between the two maps is indicated by the numbers in the circles. The pink dash line corresponds to the employed RDG isovalue.

Prior to plotting NCI map, analysis code needs to calculate values of RDG and

$sign(\lambda_2)\rho$ for a large number of grid points that evenly distributed in a rectangular region, which should be set appropriately to guarantee that all RDG isosurfaces of interest occur inside of it. A scatter map between RDG and $sign(\lambda_2)\rho$ of these grid points can be drawn to better understand the nature of the NCI map, and this kind of map is often discussed in the literatures using NCI analysis. Fig. 3(b) presents the scatter map corresponding to the grid data of Fig. 3(a). From this figure one can find four evident spikes, each one is composed of a number of points and reaches to the bottom of the graph. By comparing the colors, the correspondence between the isosurface map and scatter map can be identified, as marked by the numbers in circles in the two maps. The bottommost point of each spike essentially corresponds to the position where the electron density gradient is zero, actually it just corresponds to the CP of AIM theory. The pink dash line in Fig. 3(b) corresponds to RDG of 0.5, as can be seen it only intersects with the aforementioned four spikes, this is why the isosurfaces of RDG = 0.5 in Fig. 3(a) are able to reveal all the weak interactions. Decreasing the isovalue of RDG to a value lower than 0.5 is also acceptable, however if the value is set to be too low, the RDG isosurfaces in NCI map will become too small to be easily examined. The RDG isovalue for plotting NCI map should also not be too large, otherwise undesirable isosurfaces may occur and severely interfere with the visual analysis on the weak interactions of interest. For example, as can be seen from Fig. 3(b), if isovalue of RDG is set to be larger than about 0.7, the corresponding pink dash line in the scatter map will intersect with the grid points of no obvious meaning, thus resulting in appearance of unexpected isosurfaces.

More application examples of NCI method are given in Fig. 4 to further illustrates its capability and important value. Fig. 4(a) is a local region of halogen-bonded infinite linear chains studied in Ref. [30]. The X-bonds are all well revealed, and the light blue color implies that the interaction strength is evidently stronger than common vdW interactions. Fig. 4(b) shows sodium formate, the blue regions in the isosurface exhibit the ionic bonds between Na^+ and the negatively charged oxygens. Isosurface in Fig. 4(c) reveals the π-hydrogen bond between the hydrogen fluoride and benzene molecules.

The green color on the isosurface implies that this kind of H-bond strength is evidently lower than the H-bond in the phenol dimer we investigated earlier. Fig. 4(d) is a dihydrogen-bond complex, the hydrogen at left side carries prominent negative charge because of very small electronegativity of the lithium atom bonded to it, while the hydrogen at right side possesses considerable positive charge due to the very large electronegativity of the fluorine atom. As a result, there is a strong electrostatic attraction between the two hydrogens, the blue isosurface between the LiH and HF nicely reveals this nature. Note that since the Li-H bond shows significant ionicity and the ρ in the bonding region is quite low, this bond is also revealed by a corresponding RDG isosurface. Cyclo[18]carbon is a very unusual molecule,[31, 32] and its interaction with various small molecules was comprehensively studied by us recently.[12] Fig. 4(e) presents NCI map of a complex formed by carbon monoxide and the cyclo[18]carbon, the green circular isosurface intuitively reveals that the carbon monoxide is attracted by all carbons in the ring through vdW interaction. Fig. 4(f) shows NCI map of a long alkane $C_{17}H_{36}$ in optimal conformation, the prominent dispersion interaction between the two segments can be detected very easily. It is worth to note that Ref. [33] indicated that for linear alkane systems, when the chain length is long enough, such as the $C_{17}H_{36}$ we investigated here, the hairpin conformation have lower energy than straight conformation due to prominent intramolecular dispersion interaction. Fig. 4(g) presents NCI map for σ-bonded nonacene dimer, which was theoretically investigated in detail in Ref. [34]. In this map, not only the green isosurfaces well unveil the considerable large area π-π stacking interactions, but also the brown and red isosurface regions vividly exhibit the remarkable steric hindrance effect around the center of the dimer.

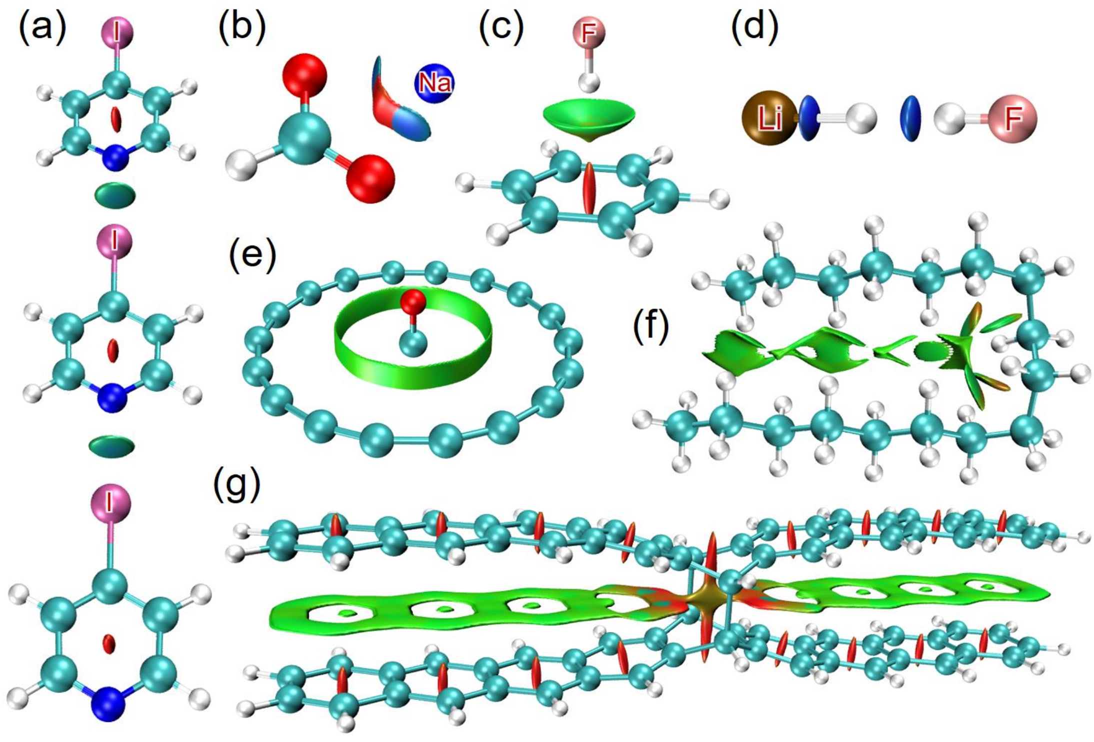

Fig. 4 NCI map of various systems. $sign(\lambda_2)\rho$ is mapped on the RDG isosurfaces according to the color bar in Fig. 2. If not explicitly labelled, blue, red, cyan and white atoms correspond to nitrogen, oxygen, carbon and hydrogen, respectively.

NCI analysis can also be employed for visual studying weak interactions in periodic systems, and this has been supported in Multiwfn and Critic 2 codes.[24, 35] Three examples are given in Fig. 5. Fig. 5(a) presents NCI map of boron nitride, which is a two-dimensional system with noticeable vdW interactions between the layers. The isosurfaces not only correctly show this feature but also display the steric effect within six-membered rings in each layer. The green RDG isosurfaces in Fig. 5(b) clearly display the vdW interaction between neighbouring C_{60} fullerenes in the crystal environment. For clarity, the central and surrounding fullerenes are drawn in opaque and transparent styles, respectively, and the uninterested isosurfaces representing the steric effect within the fullerenes are shielded by manually setting RDG in the regions where $sign(\lambda_2)\rho$ larger than 0.01 a.u. to an arbitrary large value. The system in Fig. 5(c) is a representative two-dimensional covalent organic framework (COF) compound, and its layers show evident π-conjugation character. As can be seen from the figure, the green RDG isosurfaces convincingly reveal that there is an infinitely extended π-π stacking between the two layers in the cell; at the same time, the steric effects, vdW interactions and H-bonds in each layer are also well exhibited by red, green and blue isosurfaces, respectively.

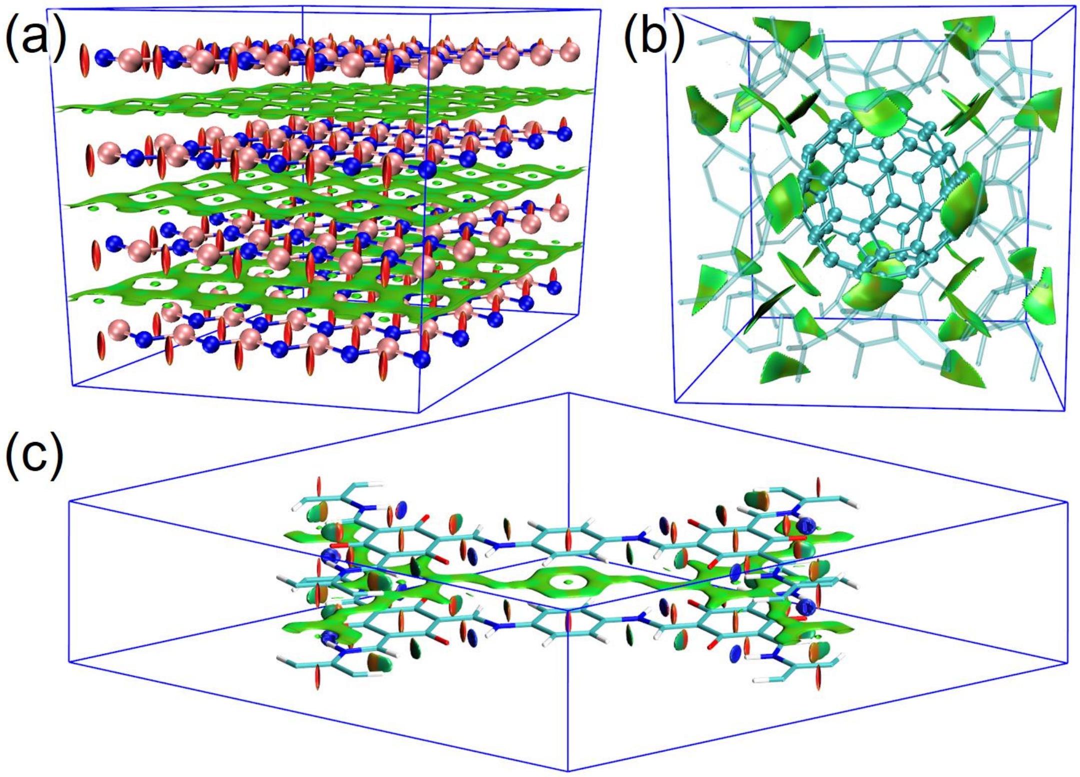

Fig. 5 NCI map of three crystal systems, (a) boron nitride (b) fullerene (c) covalent organic framework compound. $sign(\lambda_2)\rho$ is mapped on the RDG isosurfaces according to the color bar in Fig. 2. Cell border is portrayed by blue box. For clarity, when plotting (b), the RDG isosurfaces in the regions where $sign(\lambda_2)\rho$ is larger than 0.01 a.u. are shielded; when plotting (a) and (c), the periodicity in the direction perpendicular to the layers is ignored.

2.3 Relationship between NCI method and AIM theory

The relationship between NCI analysis and the widely employed AIM topology analysis is worth to mention. In AIM theory, BCP is often recognized as the most representative position of a notable interaction, and values of various functions at a BCP are very useful in characterizing the interaction nature and strength. Bond path is generated by tracing the steepest ascent path from a BCP, and it may be viewed as the most representative path revealing an interatomic interaction. In most cases, each RDG isosurface contains at least one point with vanished electron density gradient, which corresponds to a CP in AIM theory. BCP can always be found on a RDG isosurface, and the accompanied bond paths always cross RDG isosurfaces. In this regards, NCI analysis may be regarded as a visual extension of AIM theory.

Fig. 6 presents a NCI map with the BCPs and bond paths generated by AIM topology analysis for stacked guanine-cytosine base pairs. For the three H-bonds within each layer of the base pair, the information at the BCPs can be used in quantitative analysis of bonding character, while the RDG isosurfaces graphically display the bonding regions and exhibit the magnitude of ρ. It is obvious that AIM and NCI are complementary to each other in quantitative analysis and qualitative visual inspection. While for the π-π stacking vividly shown by the wide green RDG isosurfaces, the AIM analysis is no longer useful, since the corresponding discretely distributed BCPs can hardly reveal the very broad areas where the π-π stacking actually occurs. Therefore, NCI analysis has an evidently irreplaceable value in analyzing certain kinds of interactions with respect to AIM.

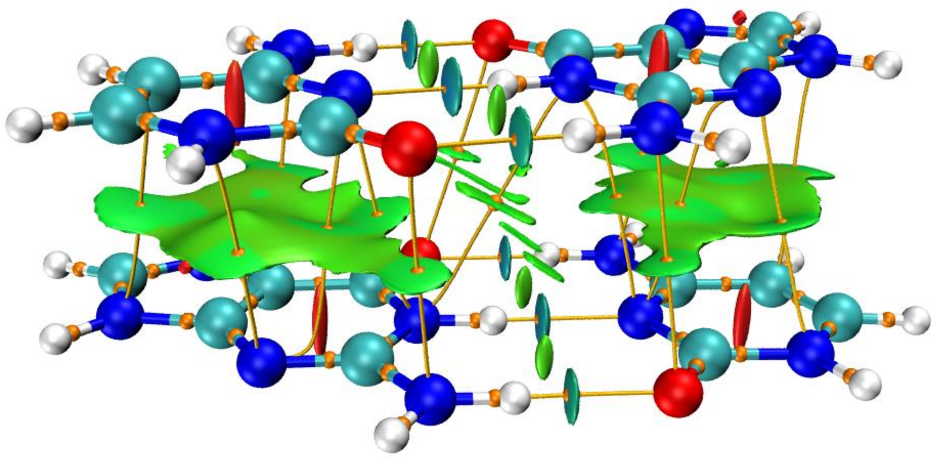

Fig. 6 NCI map with bond critical points (orange spheres) and bond paths (yellow lines) of two layers of guanine-cytosine base pair. $sign(\lambda_2)\rho$ is mapped on the RDG isosurfaces according to

the color bar in Fig. 2.

Furthermore, NCI has capacity of revealing some important interactions that fully hidden in AIM topology analysis. For example, it was shown that some prominent intramolecular H-bonds do not have corresponding BCPs,[36] and recently we provided a detailed theoretical analysis on the underlying reason.[37] The $Ni(NH_3)_2(OH)_2$ transition metal coordinate in Fig. 7 is a typical instance of this situation. It can be seen that there is no BCP corresponding to the intramolecular H-bonds between the $-NH_3$ and -OH ligands, while the blue region of the RDG isosurfaces clearly demonstrates the existence of the H-bonds. Also, the red region depicts the steric repulsion between the ligands due to their close contact. Corresponding scatter map between RDG and $sign(\lambda_2)\rho$ of the grid points for plotting the NCI map is also given in Fig. 7. It can be seen that the two spikes respectively corresponding to the H-bond and steric interactions do not reach to the bottom of the map, that is, there is no position in the interaction regions with vanished gradient norm of ρ, and thus CP cannot be found. All weak interactions with similar character cannot be investigated by AIM topology analysis at all, but need to be studied by NCI or related analysis methods described later.

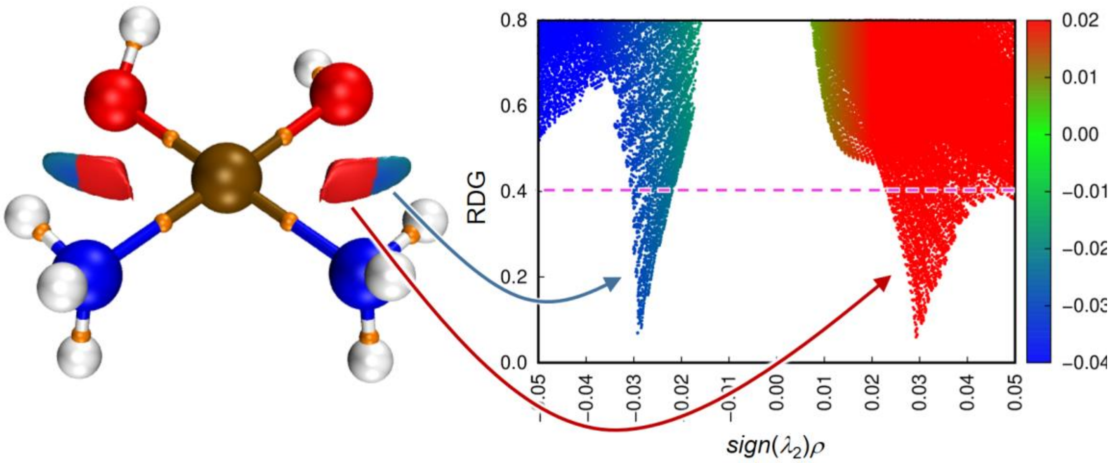

Fig. 7 NCI map with bond critical points (orange spheres) of $Ni(NH_3)_2(OH)_2$. $sign(\lambda_2)\rho$ is mapped on the RDG = 0.4 isosurfaces according to the color bar in Fig. 2. Corresponding scatter map between RDG and $sign(\lambda_2)\rho$ is also given, the pink dash line corresponds to the isovalue

of RDG in the NCI map.

2.4 Quantitative analysis under the NCI framework

The original purpose of NCI method is only to visually reveal weak interactions regions. Later, some people considered quantifying strength of the interactions described by RDG isosurfaces, and then proposed q_{bind} index. In Ref. [38], it was demonstrated that for a H-bond dimer, the scan curve of this index well mimics actual potential energy curve. The definition of q_{bind} is

$$q_{\text{bind}} = -(q_{\text{att}} - q_{\text{rep}}) \tag{2}$$

where the q_{att} and q_{rep} characterize attractive and repulsive effects, respectively

$$\begin{aligned} q_{\text{att}} &= \int_{\Omega_{\text{NCI}}} \rho^n(\mathbf{r})\,\mathrm{d}\mathbf{r} \qquad \lambda_2(\mathbf{r}) < 0 \\ q_{\text{rep}} &= \int_{\Omega_{\text{NCI}}} \rho^n(\mathbf{r})\,\mathrm{d}\mathbf{r} \qquad \lambda_2(\mathbf{r}) > 0 \end{aligned} \tag{3}$$

As mentioned earlier, the sign of λ_2 can be utilized to discriminate interaction types, so the q_{att} and q_{rep} correspond to integrating in the subregions where λ_2 is smaller and larger than 0 within the RDG isosurface of interest, respectively. It was shown that for isosurface of RDG = 0.6, the case of n = 4/3 gives best correlation between q_{bind} and the actual potential curve obtained by quantum chemistry calculation. Recently, a similar method based on integrating ρ^n was proposed to analyze conformation energies of biomolecular systems.[39, 40] Tests found that the frames in molecular dynamics (MD) simulation with lower energy tend to have a large integral value.

Besides, in Ref. [41], it was found that the volume in the region where RDG is smaller than 0.5 and ρ is smaller than 0.05 a.u. has somewhat correlation with relative energies between different configurations or conformations of a few organic systems. It was observed that generally, the lower the energy, the larger the volume, which implies larger interaction area.

Despite the evidences mentioned above, NCI analysis can be correlated with energy in terms of integration of specific functions in specific regions defined by RDG, in our own viewpoint, it is unlikely possible to define a general index simply based on the integration to accurately estimate interaction energy between molecules or predict energy difference between various structures, since there are so many kinds of interaction in chemical systems with very different natures, while the information provided in the current NCI framework is limited. For example, ρ in the bonding region of an ionic bond and a H-bond often has similar magnitude, but strength of the two kinds of bonds often differs by one order of magnitude, clearly integral of ρ (or its variants) within the corresponding RDG isosurfaces cannot distinguish their huge difference in interaction energies. However, we believe that it is promising to take the indices obtained by the aforementioned NCI integration method as descriptors to train machine learning potential that suitable for specific systems.

2.5 NCI analysis based on promolecular approximation (NCI^{pro})

The NCI analysis can also be conducted under the so-called promolecular approximation,[23] namely the ρ involved in the analysis is replaced with promolecular density, ρ^{pro}. We will refer this special form of NCI analysis to NCI$^{\mathrm{pro}}$. The ρ^{pro} can be constructed extremely easily and rapidly, since it simply corresponds to superposition of spherically averaged densities of all atoms in the system in their isolated states, that is $\rho^{\mathrm{pro}} = \sum_i \rho_i^{\mathrm{free}}$. The spherically averaged free-state atomic densities ρ^{free} for different elements were precalculated by developers and embedded in analysis code. They can be fitted using analytic functions such as Slater type orbitals (STOs), or tabulated at specific radial distances and then employing interpolation technique to estimate the value and derivatives at given distances. The key advantage of NCI$^{\mathrm{pro}}$ is that its calculation speed is about two or even more orders of magnitude faster than NCI. In the highly optimized Multiwfn program, NCI$^{\mathrm{pro}}$ can even be applicable to systems with thousands of atoms, such as biomacromolecules. In addition, since NCI$^{\mathrm{pro}}$ is solely dependent of atomic coordinates, it is more convenient to use than NCI, because users only need to provide a file containing a reasonable geometry structure as input, which may come from e.g. experimental determination and molecular force field minimization.

Compared to actual ρ, the ρ^{pro} fully ignores variation of electron distribution during formation of practical chemical system from isolated atoms caused by various electronic effects such as charge transfer, polarization and Pauli repulsion. Despite of this, using ρ^{pro} in NCI analysis is still generally meaningful and acceptable, since distribution of electron density in weak interaction region is often not significantly influenced by electronic effects. In most cases, the information about weak interactions conveyed by NCI$^{\mathrm{pro}}$ map is coincident with NCI map.[23, 41] However, graphical effect of NCI$^{\mathrm{pro}}$ is somewhat poorer than NCI, and because the NCI$^{\mathrm{pro}}$ analysis does not take actual electronic structure into account, its robustness and physical meaning are inevitably not as good as NCI. Therefore, whenever cost of NCI analysis is affordable, we always recommend to use NCI.

Recently NCI-ELMO method was proposed.[42] This strategy performs NCI analysis for proteins based on the ρ approximately constructed by simple combination of density matrix of amino acid residues, which are available in a pre-built library. Therefore, extremely expensive quantum chemistry calculation for the whole protein is avoided. Compared to the NCI$^{\mathrm{pro}}$, it was found that NCI-ELMO always has a better result. We note that if only the weak interactions in a local region of the whole protein is really of interest, in fact one can truncate the protein to construct a cluster model,[43] which usually contains about 100 to 300 atoms, then there will be not difficulty to perform a routine quantum chemistry calculation and then NCI analysis.

2.6 Some notes on conducting NCI analysis

In this section we provide some notes and cautions on performing NCI analysis based on our long-term experience.

The geometry used in NCI and related analyses introduced in later sections is worth to mention. The geometry structure should be optimized at an appropriate level, otherwise the electronic structure of the system may be highly artificial, leading to misleading conclusion from the NCI analysis. For example, it is well-known that argon dimer is formed by vdW attraction. At its equilibrium geometry (approximately 3.76 Å[44]), the RDG isosurface between the two atoms is fully green, indicating the very low ρ in the interaction region. However, at the Ar-Ar distance of 2.7 Å where the two atoms are obviously mutually repulsive, the isosurface showing the interaction is blue, as if there is a strong attractive interaction in this situation. This misleading observation comes from the fact that when two atoms are forced to occur very closely to each other, the ρ in their overlapping area will inevitably be greater than the case of equilibrium structure. Evidently, the relatively large ρ in this case is never a direct evidence of inherent strong attraction between the atoms.

If the geometry for NCI analysis is taken from X-ray crystal diffraction experiment and the resolution is satisfactory, and meantime one intends to study weak interactions in crystal environment, then optimization of non-hydrogen atoms can be avoided, but positions of hydrogens still need to be refined by geometry optimization, especially when H-bonds are of interest. This is because commonly coordinates of hydrogens cannot be accurately determined by X-ray diffraction.[45]

In most cases, the ρ and its derivatives involved in NCI analysis are estimated based on electronic wavefunction produced by quantum chemistry (for isolated systems) or first-principle (for periodic systems) calculations. According to our experience and benchmark in Ref. [41], NCI analysis has low sensitivity to quality of wavefunction. Also, it is widely known that geometry optimization is not very demanding on calculation level. Therefore, a common practice of performing NCI analysis is using density functional theory (DFT) in combination with a medium-sized basis set to optimize the structure, and the wavefunction corresponding to the converged geometry will be subjected to NCI analysis. The exchange-correlation functional employed in DFT calculation should be capable of reasonably representing dispersion effect, otherwise the optimized geometries may be meaningless when the geometry is heavily influenced by dispersion interaction. Usually we recommend B3LYP-D3(BJ)[46, 47] and ωB97XD[48] functionals for isolated systems, since they are inexpensive, popular, robust and widely supported by quantum chemistry programs. While for periodic calculations, since hybrid functionals are often significantly more computationally demanding than pure functionals, we generally recommend to use the popular PBE-

D3(BJ)[46, 49] and TPSS-D3(BJ).[46, 50] Using more higher level of theoretical methods, such as double-hybrid functionals[51] or coupled-cluster singles and doubles (CCSD)[52] to optimize geometry or derive ρ, is completely unnecessary for NCI analysis. As for the basis set, 3-zeta basis sets without the expensive high angular momentum polarization functions are good choices, for example, 6-311G**[53] and def-TZVP.[54] Further increasing basis set quality does not bring detectable benefit to the result. Using a cheaper 2-zeta basis set containing polarization functions such as 6-31G**[55] and def2-SVP[56] is also fully acceptable. The B97-3c[57] and r^2SCAN-3c[58] are also worth to recommend for NCI analysis purpose. They are low-cost composite methods combining a pure functional, a medium-sized basis and some additional empirical corrections. When RIJ technique[59] is utilized to accelerate the integral evaluations in their calculations, they can be efficiently employed for geometry optimization and generation of wavefunction for relatively large system. We found quality of wavefunction at these two levels is satisfactory for NCI and related analyses.

GFN-xTB theory[60, 61] becomes increasingly popular in recent years, which can be regarded as a semi-empirical version of DFT method. The GFN-xTB in xtb code[62] is able to easily optimize a system containing hundreds or even a thousand atoms on a personal computer, and the generated wavefunction recorded in Molden format can be used in Multiwfn code for NCI analysis. According to our tests, if only qualitatively reasonable NCI map is needed, the wavefunction generated by the extremely fast GFN-xTB method can be adopted for most cases.

The graphical quality of NCI map is very sensitive to the quality of grid data of RDG and $sign(\lambda_2)\rho$, which is reflected by spacing between grid points. Too large grid spacing will result in unsightly jagged edges on the RDG isosurfaces. However, if the grid spacing is too small, it will cause too much computational cost. Note that if spatial range of the grid data is fixed, the time spent in calculating the grid data is inversely proportional to the third power of the grid spacing. According to our experience, grid spacing of 0.2 Bohr is usually the lowest acceptable grid quality for NCI map; if one has a high requirement on graphical quality, grid spacing evidently lower than 0.15

Bohr should be used.

Spatial range of the grid data should be properly set before starting calculation. The general guidance is that the spatial range should fully cover all regions where the isosurfaces corresponding to interested weak interactions may occur, otherwise some isosurfaces may be missing or truncated. For example, if weak interactions are spread over the whole system, and one want to reveal all of them in the NCI map at the same time, the range of grid data should cover the entire system. In contrast, if the weak interaction of interest occurs only in a local region of a large system, then one can properly define the spatial range so that the grid points will only distribute in the areas of interest, which not only considerably reduces computational time, but also avoids the appearance of the isosurfaces in irrelevant area.

The choice of color scale of $sign(\lambda_2)\rho$ has arbitrariness to some extent. The color scale given in Fig. 2, namely from -0.04 to 0.02 a.u., is suitable for general cases, but may be adjusted appropriately. For example, if a RDG isosurface corresponding to a H-bond shows light blue color, while one wants its color to appear more vivid in the map, the lower limit of color scale can be slightly increased to -0.035 a.u., the blue on the isosurface will become slightly darker.

The isovalue used to plot RDG isosurfaces can also be adjusted properly to improve graphical quality according to actual situation. RDG of 0.5 is a reasonable choice for most cases. Often it can be slightly increased to 0.6, the isosurfaces will become wider and easier to inspect. However, if the value is set too large, it will cause meaningless and messy isosurfaces.

3 DORI and IRI methods: Revealing all kinds of interactions

As illustrated in Fig. 1, NCI map cannot simultaneously well represent weak interactions and the chemical bond interactions with notable covalent character even if truncation of ρ is not considered. In order to exhibit covalent and noncovalent interactions in a single map, Piquemal et al. suggest plotting isosurfaces of RDG and electron localization function (ELF) together, since ELF has a strong capacity of revealing covalent interactions.[63-65] The combination use of RDG and ELF indeed has certain practical significance, however, considering two functions in an analysis is obviously inconvenient.

Silva and Corminboeuf defined a function named density overlap regions indicator (DORI), which aims at revealing covalent and noncovalent interactions in an equal footing. DORI is expressed as

$$\mathrm{DORI}(\mathbf{r}) = \frac{\theta(\mathbf{r})}{1+\theta(\mathbf{r})} \tag{4}$$

where

$$\theta(\mathbf{r}) = \frac{\left\{ \nabla \left[\frac{\nabla \rho(\mathbf{r})}{\rho(\mathbf{r})} \right]^2 \right\}^2}{\left[\frac{\nabla \rho(\mathbf{r})}{\rho(\mathbf{r})} \right]^6} \tag{5}$$

The value range of DORI is [0,1] because of its mathematical form in Eq. 4. If isovalue of DORI is chosen properly, all kinds of interactions in a system could be unveiled by DORI isosurfaces. However, the graphical effect of DORI map is not satisfactory, the complicated definition of DORI leads to very complex variation behavior of this function and numerical instability.

By careful examining the graphical character and definition of RDG, we found that both weak and strong interactions can be represented equally well by a trivial modification on RDG, which results in a new function named interaction region indicator (IRI),[37]

$$\mathrm{IRI}(\mathbf{r}) = \frac{|\nabla \rho(\mathbf{r})|}{[\rho(\mathbf{r})]^a} \tag{6}$$

in which the empirical parameter a is chosen to be 1.1 to best balance the graphical representation of various kinds of interactions. By comparing Eqs. 1 and 6, it can be found that RDG and IRI only differ by the parameter a and a constant prefactor. Although IRI does not have a fixed value range like DORI, we found isovalue of 1.0

a.u. is able to give rise to ideal graphical effect for most cases, though the isovalue could be properly varied between 0.8 to 1.2 to try to improve graphical representation according to practical situation.

Despite the definition of IRI is significantly simpler than DORI, the IRI map always has an evidently better graphical effect than DORI. In particular, the noisy and discrete isosurfaces in DORI map are fully avoided. In analogy with NCI analysis, $sign(\lambda_2)\rho$ can also be mapped on IRI or DORI isosurfaces by different colors to visually characterize nature of the interactions.

As a byproduct of IRI analysis, we proposed IRI-π function,[37] which corresponds to the IRI by only taking π electrons into account. It is found that the shape of IRI-π isosurfaces and the magnitude of ρ mapped on them have good capability of distinguishing type and strength of π interactions.

To illustrate the unique ability of IRI map in revealing interactions, we respectively provide IRI map of zirconocene dichloride and a dimer containing two chalcogen bonds as Figs. 8(a) and 8(b). From Fig. 8(a), it is clear that all kinds of interactions in the coordinate have been fully exhibited by corresponding IRI isosurfaces, including the Zr-Cl and Zr-C coordinate bonds, the C-H and C-C bonds in the cyclopentadienyl ligands, as well as the vdW interaction and steric effect between the ligands. At the meantime, the natures of these interactions are well distinguished by the $sign(\lambda_2)\rho$ mapped on the isosurfaces. The Te-containing chalcogen bond dimer in Fig. 8(b) was studied by Kraka et al.,[7] the intramolecular Te-N, N-C, C-C and C-H bonds are all displayed by dark blue isosurfaces, the color reflects that the $sign(\lambda_2)\rho$ in the bonding regions is very negative, which corresponds to significant attractive interaction of the chemical bonds. On the IRI isosurface between the two molecules in Fig. 8(b), two blue zones can be clearly observed, their appearances imply that the two Te···N chalcogen bonds are by far stronger than common vdW interactions. It is worth to note that formation of such a relatively high-strength weak interaction is usually driven by electrostatic attraction and assisted by orbital interaction.[1, 7] The red region in the intermolecular IRI isosurface in Fig. 8(b) shows that formation of the closely contacted dimer configuration driven by the strong chalcogen bonds results in occurrence of remarkable steric repulsion, which must have a certain offsetting effect on the dimer binding.

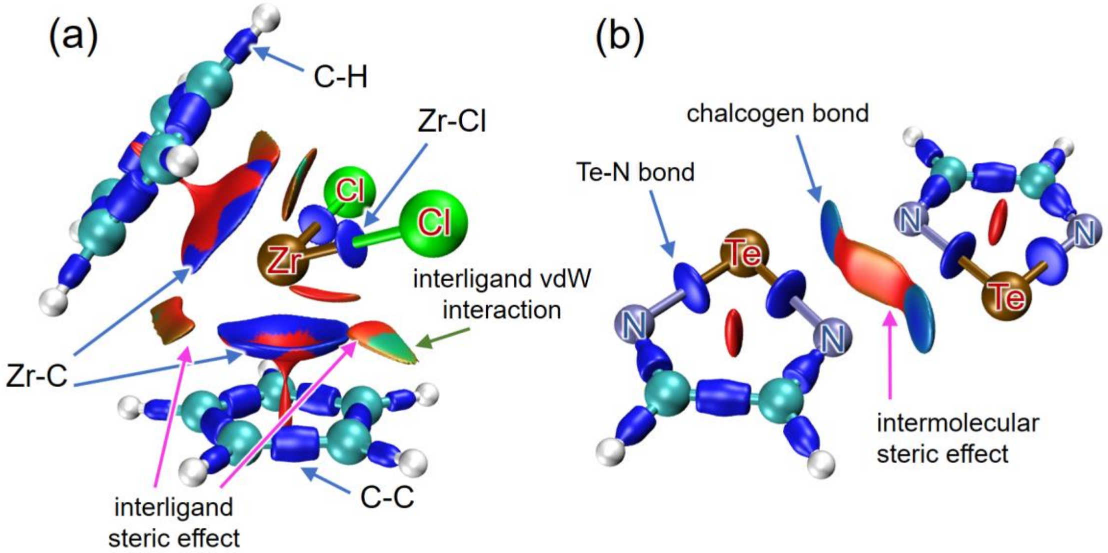

Fig. 8 IRI map of (a) zirconocene dichloride (b) Te-containing chalcogen bond dimer. $sign(\lambda_2)\rho$ is mapped on the isosurfaces according to the color bar in Fig. 2. Isovalue of IRI for (a) and (b) are set to 0.8 and 1.0 a.u. for best graphical effect, respectively.

IRI analysis is also particularly useful in understanding interactions in solid and surface systems. Fig. 9 is an example of using IRI to investigate reconstruction effect of Si(001) surface. Figs. 9(a) and (b) show the Si(001) surface before and after the reconstruction, respectively. It can be seen that the reconstruction leads to formation of new Si-Si bonds between adjacent Si atoms at the top of the surface. Fig. 9(c) is IRI map of reconstructed Si(001) surface, in which the original and newly formed Si-Si bonds are all clearly revealed by the blue cylindrical IRI isosurfaces. In addition, weak interactions in the Si(001) surface are also well portrayed. The green slim IRI isosurfaces represent the vdW interactions originally exist in the cavity of the silicon crystal, while the wide red IRI isosurfaces fully show the occurrence of noticeable steric hindrance in the newly formed cages due to the surface reconstruction. Obviously, the spontaneous of reconstruction of the surface is accompanied by a decrease in the total energy of the system, while the newly emerging steric hindrances must hinder the progress of the reconstruction and positively contribute to energy variation.

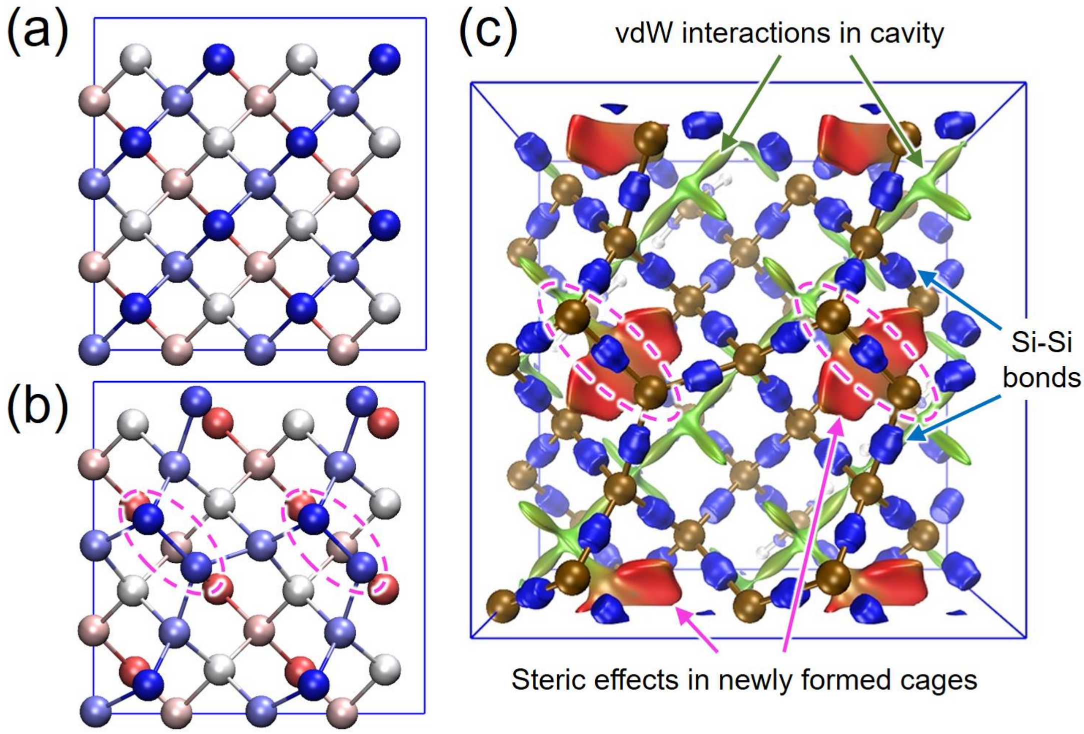

Fig. 9 (a) and (b): Si(001) surface before and after surface reconstruction, respectively. Si atoms at top, middle, and bottom of the surface are rendered by blue, white and red, respectively. (c) IRI map of reconstructed Si(001) surface. $sign(\lambda_2)\rho$ is mapped on the IRI isosurfaces according to the color bar in Fig. 2. Pink dash circles highlight the newly formed Si-Si bond due to the reconstruction

IRI can not only show strong and weak interactions at the same time, but also nicely portray the smooth transition between them, this feature makes IRI very suitable for investigating change of bonding during a chemical process. As an example, Fig. 10 presents IRI maps of representative points in intrinsic reaction coordinate (IRC) path of ethanol dehydration process. From the variation of shapes and colors of the IRI isosurfaces in these maps one can recognize that the reaction consists of the following processes: As the oxygen atom and a hydrogen atom of the methyl group gradually approach with each other, a notable vdW interaction first appears between them, then it becomes a significant intramolecular H-bond, and finally it forms an ordinary chemical bond. At the same time, the C-O and C-H bonds gradually elongate. After passing through the transition state, their strengths gradually reduce to weak interaction category. At the end of the reaction, only a weak π-hydrogen bond remains between the two product molecules, namely the water and the ethylene. More examples of using IRI to analyze chemical processes can be found in Ref. [37], and in the supplementary information of that paper, animation files showing evolution of IRI map for the studied reactions are provided, which represent the whole studied reaction processes in a quite vivid manner.

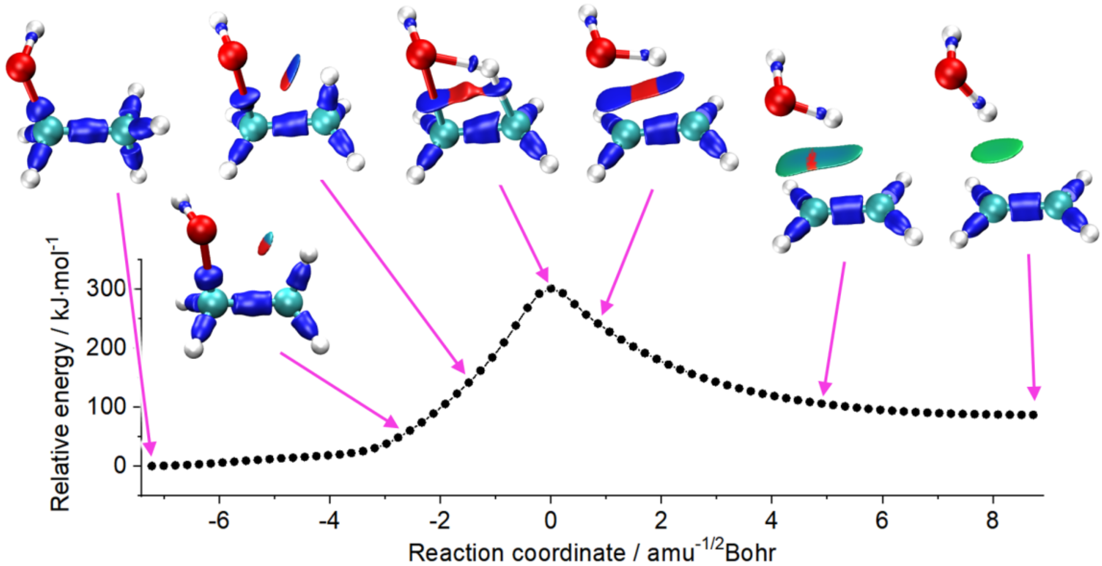

Fig. 10 Evolution of IRI map of ethanol dehydration process $CH_3CH_2OH \rightarrow C_2H_4 + H_2O$. $sign(\lambda_2)\rho$ is mapped on the IRI isosurfaces according to the color bar in Fig. 2. Each black point corresponds to a structure in intrinsic reaction coordinate.

4 IGM method: Separately revealing intrafragment and interfragment interactions

The independent gradient model (IGM) originally proposed by Hénon et al. in 2017 is a visual analysis method for studying both weak and strong interactions.[66, 67]

Then during our implementation of IGM in Multiwfn code, we also made some extensions in its methodology. In the aspect of revealing weak interactions, a key advantage of IGM over NCI and NCI^{pro} is that intrafragment and interfragment interactions can be completely isolated in an elegant way.

To easily understand how IGM method works, we first look at a very simple linear system, hydrogen molecule. At its equilibrium structure, the density distributions of the two hydrogens in their free-state along the molecular axis is shown in Fig. 11(a), the sum of the two atomic densities corresponds to promolecular density, whose gradient (g) is given by the black curve in Fig. 11(b). From Fig. 11(a) one can find that the density gradients of the two hydrogens in their bonding region have opposite signs, one is positive while another one is negative. Therefore, in Fig. 11(b), the contributions from the two atoms to g largely cancel with each other, and the g even reaches to zero at midpoint of the bond. The g^{IGM} displayed by green curve in Fig. 11(b) denotes IGM type of density gradient, which is defined as the sum of absolute value of density gradient of each atom in their free-states. Due to this character, g^{IGM} is upper limit of g. From Fig. 11(b) one can find that g^{IGM} is larger than g everywhere. The δg corresponds to the difference between g^{IGM} and g, its distribution is shown by the blue curve in Fig. 11(b). It is seen that δg is relatively large between the two atoms, and reaches maximum at their midpoint. Due to this distribution behavior of δg, IGM method employs δg to reveal interaction regions via its isosurfaces. For example, according to the two intersections between the dash line and the δg curve in Fig. 11(b), it can be easily recognized that the H-H bond can be revealed by δg isosurface of 0.2 a.u. It is worth to mention that the height of peak of δg in an interaction region was found to have a positive correlation with the interaction strength.[66]

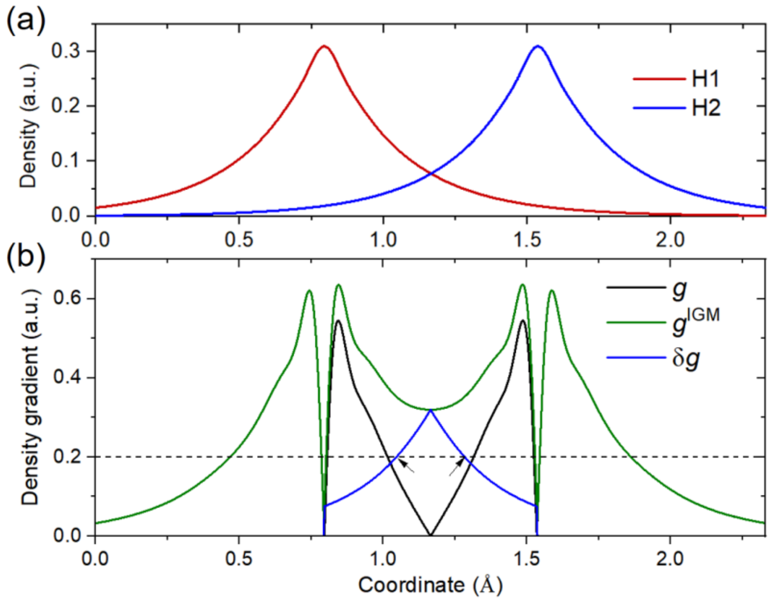

Fig. 11 Electron density along axis of hydrogen molecule at its equilibrium structure. (a) Free-state densities of the two hydrogen atoms (b) Gradient of promolecular density (g), IGM type of density gradient (g^{IGM}), and their difference (δg). The two arrows indicate the intersections between the dash line of Y=0.2 and the δg curve.

For a general, three-dimensional case, δg can be expressed as[68]

$$\delta g(\mathbf{r}) = g^{\mathrm{IGM}}(\mathbf{r}) - g(\mathbf{r}) \tag{7}$$

where

$$\begin{aligned} g(\mathbf{r}) &= \left| \sum_i \nabla \rho_i^{\mathrm{free}}(\mathbf{r}) \right| \\ g^{\mathrm{IGM}}(\mathbf{r}) &= \sum_i \left| \nabla \rho_i^{\mathrm{free}}(\mathbf{r}) \right| \end{aligned} \tag{8}$$

δg has capacity to reveal all interactions in a system. In order to solely reveal interaction between specific fragments, the IGM method defines $\delta g^{\mathrm{inter}}$

$$\delta g^{\mathrm{inter}}(\mathbf{r}) = g^{\mathrm{IGM,inter}}(\mathbf{r}) - g^{\mathrm{inter}}(\mathbf{r}) \tag{9}$$

where g^{inter} is the magnitude of vector sum of density gradients of all fragments, while $g^{\mathrm{IGM,inter}}$ corresponds to the sum of magnitude of density gradient of all fragments[68]

$$g^{\text{inter}}(\mathbf{r}) = \left| \sum_{A} \sum_{i \in A} \nabla \rho_i^{\text{free}}(\mathbf{r}) \right|$$
$$g^{\text{IGM,inter}}(\mathbf{r}) = \sum_{A} \left| \sum_{i \in A} \nabla \rho_i^{\text{free}}(\mathbf{r}) \right| \tag{10}$$

in which the indices i and A loop over atoms and defined fragments, respectively. Note that the δg^{inter} essentially comes from overlap of electron density between fragments, which is an implication of occurrence of interfragment interaction.

Finally, δg^{intra} is defined as complement of δg^{inter} aiming for revealing intrafragment interactions

$$\delta g^{\text{intra}}(\mathbf{r}) = \delta g(\mathbf{r}) - \delta g^{\text{inter}}(\mathbf{r}) \tag{11}$$

In Multiwfn code, arbitrary number of fragments can be defined according to practical research purpose, and their union is not necessarily equal to the entire system. This flexibility in fragment partition makes analysis of interfragment interaction extremely convenient and controllable.

In an interaction region at optimized geometry, the magnitude of δg usually has a loose positive correlation with interaction strength. Therefore, isovalue of δg (or δg^{inter} and δg^{intra}) should be properly selected when plotting IGM maps. When the isovalue is set to a large value, only strong interactions can be represented by the isosurfaces. When the isovalue is set to a lower value, relatively weaker interactions can also be displayed, but at this time the range of the isosurfaces corresponding to the relatively strong interactions may become too wide for clear investigation.

Like other aforementioned analysis, commonly $sign(\lambda_2)\rho$ is mapped on δg, δg^{inter} and δg^{intra} isosurfaces to distinguish types of all interactions, interfragment interactions and intrafragment interactions. In standard implementation of IGM method, the $sign(\lambda_2)\rho$ based on promolecular approximation is used, however in Multiwfn code employing the $sign(\lambda_2)\rho$ corresponding to actual electron density is also supported.

Another great advantage of IGM compared to NCI is that some indices can be defined and readily calculated for quantifying contributions from atoms or atomic pairs to the interaction between two selected fragments. δG^{pair} is defined to characterize contribution of an atom pair to interfragment interaction. This index between atoms i

and j, which belong to fragments A and B respectively, is expressed as

$$\delta G_{i,j}^{\mathrm{pair}} = \int \delta g_{i,j}(\mathbf{r})\mathrm{d}\mathbf{r} = \int [g_{i,j}^{\mathrm{IGM}}(\mathbf{r}) - g_{i,j}(\mathbf{r})]\mathrm{d}\mathbf{r} \quad i \in A, j \in B \tag{12}$$

where the integration is performed numerically over the whole space, and

$$\begin{aligned} g_{i,j}(\mathbf{r}) &= \left|\nabla\rho_i^{\mathrm{free}}(\mathbf{r}) + \nabla\rho_j^{\mathrm{free}}(\mathbf{r})\right| \\ g_{i,j}^{\mathrm{IGM}}(\mathbf{r}) &= \left|\nabla\rho_i^{\mathrm{free}}(\mathbf{r})\right| + \left|\nabla\rho_j^{\mathrm{free}}(\mathbf{r})\right| \end{aligned} \tag{13}$$

In addition, percentage atomic pair contribution to interfragment interaction is defined as

$$\delta G_{i,j}^{\mathrm{pair}}(\%) = \frac{\delta G_{i,j}^{\mathrm{pair}}}{\sum_{k\in A}\sum_{l\in B}\delta G_{k,l}^{\mathrm{pair}}} \times 100\% \tag{14}$$

To quantitatively measure importance of an atom to interfragment interaction, δG^{atom} is defined. For example, contribution of atom i in fragment A to interaction between fragments A and B is evaluated as

$$\delta G_i^{\mathrm{atom}} = \sum_{j\in B}\delta G_{i,j}^{\mathrm{pair}} \tag{15}$$

and the percentage atomic contribution is evaluated as

$$\delta G_i^{\mathrm{atom}}(\%) = \frac{\delta G_i^{\mathrm{atom}}}{\sum_{j\in A}\delta G_j^{\mathrm{atom}}} \times 100\% \tag{16}$$

Obviously, if δG^{atom} or $\delta G^{\mathrm{atom}}(\%)$ is mapped on atoms by different colors, then researchers will be able to easily identify the "hot" atoms, which may play crucial role in interfragment binding. However, one should not expect that they have satisfactory capability to faithfully reveal actual atomic contribution to binding energy in general cases, after all, their definitions are quite simple and do not take any energy-related factors into account.

$\delta G^{\mathrm{inter}}$ between specific fragments is defined as integral of corresponding $\delta g^{\mathrm{inter}}$ over the whole space. It is naturally expected that this quantity could be employed as a descriptor to correlate with interaction strength. This idea has certain similarity with the NCI integration method introduced earlier.

The DNA segment in Fig. 12 is an ideal system to illustrate the unique value and features of IGM analysis. In Figs. 12(a) and 12(b), the two chains are respective defined as two fragments. Fig. 12(a) focuses on revealing H-bond interactions between the two chains, therefore $sign(\lambda_2)\rho$ colored δg^{inter} isosurfaces are plotted. As can be seen, the H-bonds are well displayed, while other interactions in the system are fully invisible in this map. In contrast, Fig. 12(b) aims at revealing interactions within each chain, therefore δg^{intra} is employed. A relatively large isovalue of δg^{intra} (0.2 a.u.) is adopted in this case, therefore only the isosurfaces corresponding to chemical bonds are shown in the figure. All δg^{intra} isosurfaces have dark blue color, this is because $sign(\lambda_2)\rho$ in the revealed chemical bond regions is significantly more negative than the lower limit of the present color scale (-0.05 a.u.). If isovalue of δg^{intra} is set to a much smaller value, for example 0.003 a.u., then weak intrafragment interactions such as π-π stacking between neighbouring bases will also be visible in the δg^{intra} isosurface map. We would like to mention in passing that IGM analysis is as cheap as NCI^{pro}. Despite this DNA segment contains as many as 638 atoms, in the Multiwfn code the computational cost for evaluating grid data for plotting Figs. 12(a) and 12(b) only takes less than one minute on a common 8-core notebook. In order to specifically study the π-π stacking between adjacent bases, we respectively defined two bases as two fragments and plotted isosurfaces of δg^{inter}, see Fig. 12(c). It is clear that existence of the stacking interaction is nicely elucidated by a flat green isosurface in this figure. In order to further quantify contributions of atoms and atom pairs to the interaction, δG^{atom} are evaluated and mapped on the atoms by different colors. The red atoms in Fig. 12(c) are those mostly participate in the interfragment interaction, while the green atoms have δG^{atom} close to zero and thus little contribute to the π-π stacking. To unveil the roles played by atomic pair interactions between the two bases, we calculated δG^{pair} among all atoms and labelled the three largest ones on Fig. 12(c). According to the values of δG^{pair} after sorting from high to low, the relative importance of the interaction between various atom pairs can be quite conveniently investigated

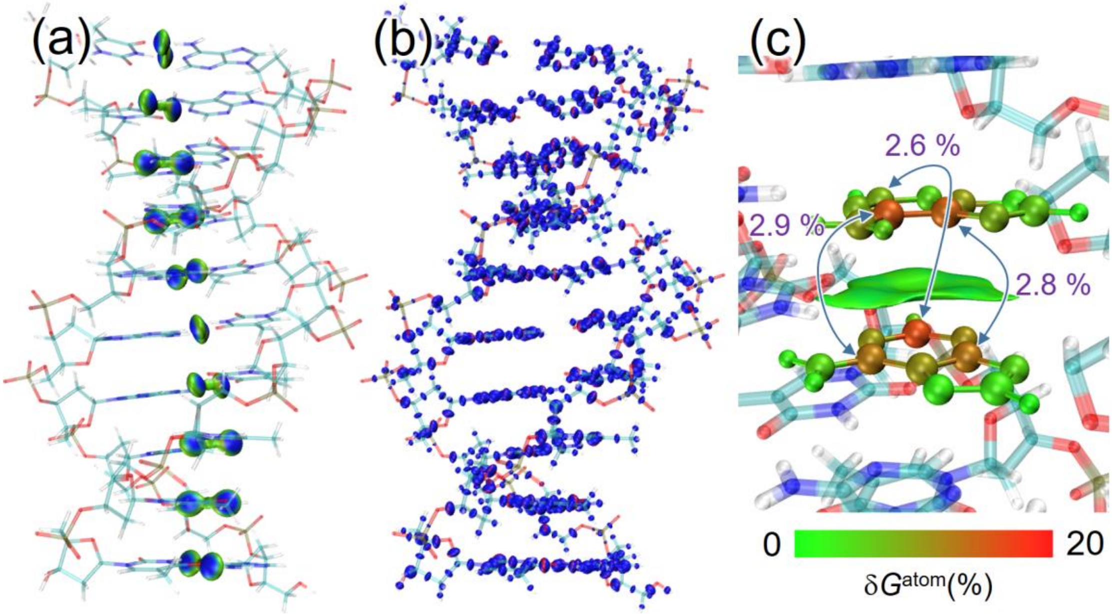

Fig. 12 IGM map of a DNA segment. (a) and (b): Two chains are respectively defined as two fragments, $sign(\lambda_2)\rho$ is colored on the δg^{inter} isosurfaces of 0.005 and 0.2 a.u. in the two maps, respectively, the coloring method is the same as Fig. 2 while color range is changed to -0.05 ~ 0.05 a.u. (c) IGM map by respectively defining two bases as two fragments. Atoms in the bases are colored according to δG^{atom}(%). Three largest δG^{pair}(%) terms are labelled in the map.

To further exhibit the powerfulness and flexibility of IGM method, we employ IGM to study a host-guest complex formed by an all-benzene trefoil knot and two hexanes, which was experimentally achieved in 2019.[69] Figs. 13(a), 13(b) and 13(c) defined fragments in the IGM analysis via different ways and plotted corresponding δg^{inter} isosurfaces. The three monomers are respectively defined as three fragments in Fig. 13(a), therefore this figure displays the vdW interactions among all the monomers. If only the interaction between the two guest molecules is of interest, then it is best to respectively define the two hexanes as the two fragments in the IGM analysis, this is exactly the situation in Fig. 13(b). It is worth to note that the isosurfaces corresponding to the vdW interaction between the two hexanes revealed by Figs. 13(a) and 13(b) are exactly the same. Fig. 13(c) collectively defines the two hexanes as a fragment while defines the trefoil knot as another fragment. Therefore, this figure only reveals the host-guest interaction. In order to visually identify the most important atoms in the trefoil knot for the host-guest interaction, the atoms in this molecule are colored by δG^{atom}(%). The red, green and blue atom colors in Fig. 13(c) vividly portray the most critical, relatively important, and insignificant atoms, respectively. For comparison purpose, NCI^{pro} map is also plotted for the present system as Fig. 13(d), in which all weak interactions are revealed simultaneously. Although this map is also of practical significance, the simultaneous appearance of isosurfaces of various interactions makes this picture too messy. For more complex three-dimensional systems, the NCI^{pro} (or NCI) map will be more inconvenient to visually investigate. Although there are some methods to realize extra processing on NCI or NCI map so as to shield the isosurfaces in uninterested area, it is distinctly not as convenient and elegant as directly employing the IGM method.

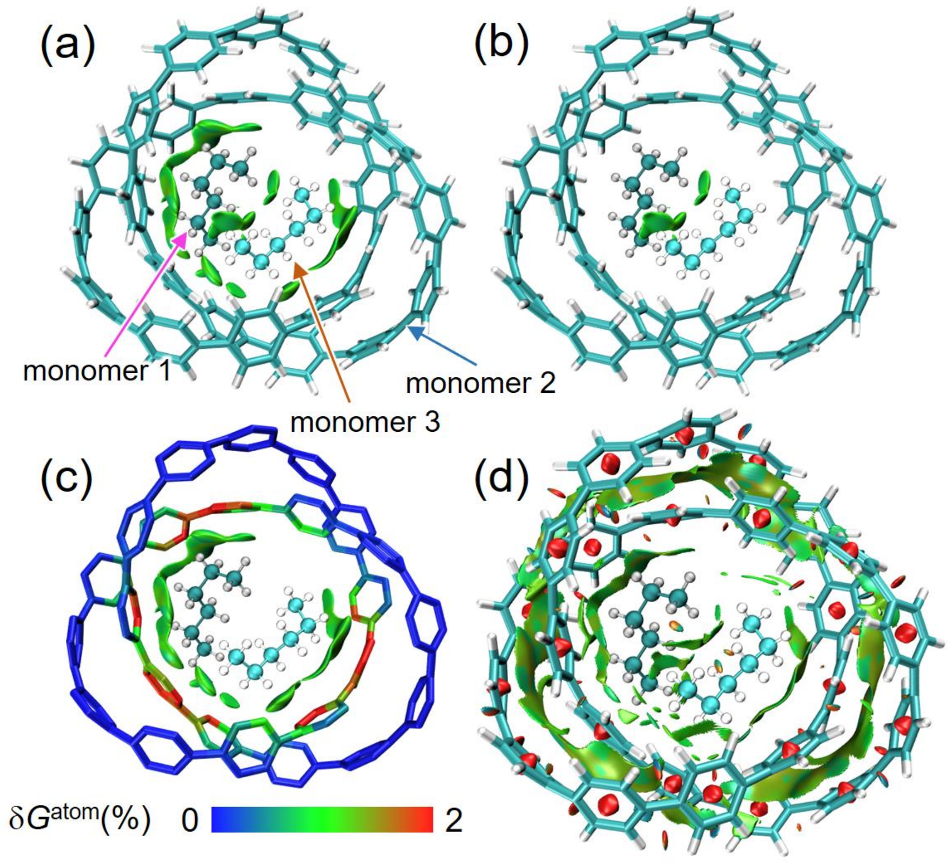

Fig. 13. Complex formed by an all-benzene trefoil knot and two hexanes. (a) IGM map defining each monomer as a fragment to reveal all intermolecular interactions. (b) IGM map only defining the two hexanes respectively as two fragments to show their interaction. (c) IGM map

defining two hexanes as a fragment and trefoil knot as another fragment to show host-guest interactions. Only non-hydrogen atoms in the trefoil knot are drawn and colored by δG^{atom}(%) to show their percentage contributions to the interaction. In all IGM maps $sign(\lambda_2)\rho$ is mapped on the δg^{inter} isosurfaces of 0.006 a.u. according to the color bar in Fig. 2 whlie color range is set to -0.05 ~ 0.05 a.u. (d) NCI^{pro} map. $sign(\lambda_2)\rho$ is mapped on the isosurfaces of RDG = 0.3 according to the color bar in Fig. 2 while color range is changed to -0.035 ~ 0.03 a.u.

5 IGMH and IGM(GBP) methods: Improvement over IGM

Since the original IGM method is only dependent of free-state atomic densities, ρ^{free}, IGM essentially belongs to a method based on promolecular approximation. We thought if it is possible to make IGM beyond the promolecular approximation to achieve a better physical meaning. Inspired by this idea, we proposed an improvement version of IGM named independent gradient model based on Hirshfeld partition (IGMH).[68] Briefly speaking, IGMH replaces all ρ^{free} involved in the IGM equations with atomic densities derived by the popular and physically meaningful Hirshfeld partition of actual electron density. The density of atom i derived in this way is expressed as $\rho_i^{\text{Hirsh}} = \rho w_i$, where ρ is the actual electron density obtained by quantum chemistry calculation, and the Hirshfeld weighting function of the atom is simply defined as[70-72]

$$w_i(\mathbf{r}) = \frac{\rho_i^{\text{free}}(\mathbf{r})}{\rho^{\text{pro}}(\mathbf{r})} \tag{17}$$

Another difference of IGMH with respect to IGM is that the $sign(\lambda_2)\rho$ calculated based on actual electron density is employed instead of the $sign(\lambda_2)\rho$ under promolecular approximation.

Since the atomic densities involved in the IGMH have stronger physical meaning than the counterpart of IGM, and better quality $sign(\lambda_2)\rho$ is employed, it is naturally expected that IGMH should have certain practical benefits over IGM in exhibiting interactions in chemical systems, indeed this is true. Figs. 14(a) and 14(b) are IGMH and IGM maps of acetic acid trimer, respectively. It can be seen that the isosurfaces in the IGM map are very bulgy and ugly. Although increasing isovalue from the 0.011 a.u. in current map to 0.015 a.u. can reduce the size of the IGM $\delta g^{\mathrm{inter}}$ isosurfaces corresponding to the H-bonds to make them look better, unfortunately in this case the isosurfaces corresponding to the vdW interactions will be unable to observe. In contrast, the existences of the H-bonds and notable vdW interactions are all elegantly represented by the IGMH $\delta g^{\mathrm{inter}}$ isosurfaces. Figs. 14(c) and 14(d) show IGMH and IGM maps of the so-called nano-Saturn formed by complexation of a nitrogen substituted [10]cycloparaphenylene ([10]CPP) nanobelt and a C_{60} fullerene.[73] The region and nature of the intermolecular interaction in this system are ideally represented by the $sign(\lambda_2)\rho$ mapped IGMH $\delta g^{\mathrm{inter}}$ isosurfaces; however, in the IGM map, the corresponding isosurfaces are partially incorrectly colored. In the region highlighted by the pink circle in Fig. 14(d), there are evident orange and cyan colors, which severely exaggerate local steric repulsion and attractive interactions between the C_{60} and [10]CPP, researchers may thus be misled by the IGM map. This problem in the IGM map comes from the fact that the IGM $\delta g^{\mathrm{inter}}$ isosurface is too thick, which has reached to the region very close to nuclei, where electron density is much larger than weak interaction regions. Note that this problem cannot be fully avoided by simply adjusting isovalue, and the problem still exists even if $sign(\lambda_2)\rho$ without promolecular approximation is mapped on the IGM $\delta g^{\mathrm{inter}}$ isosurfaces. More instances showing advantage of IGMH over IGM can be found in our original paper of IGMH.[68]

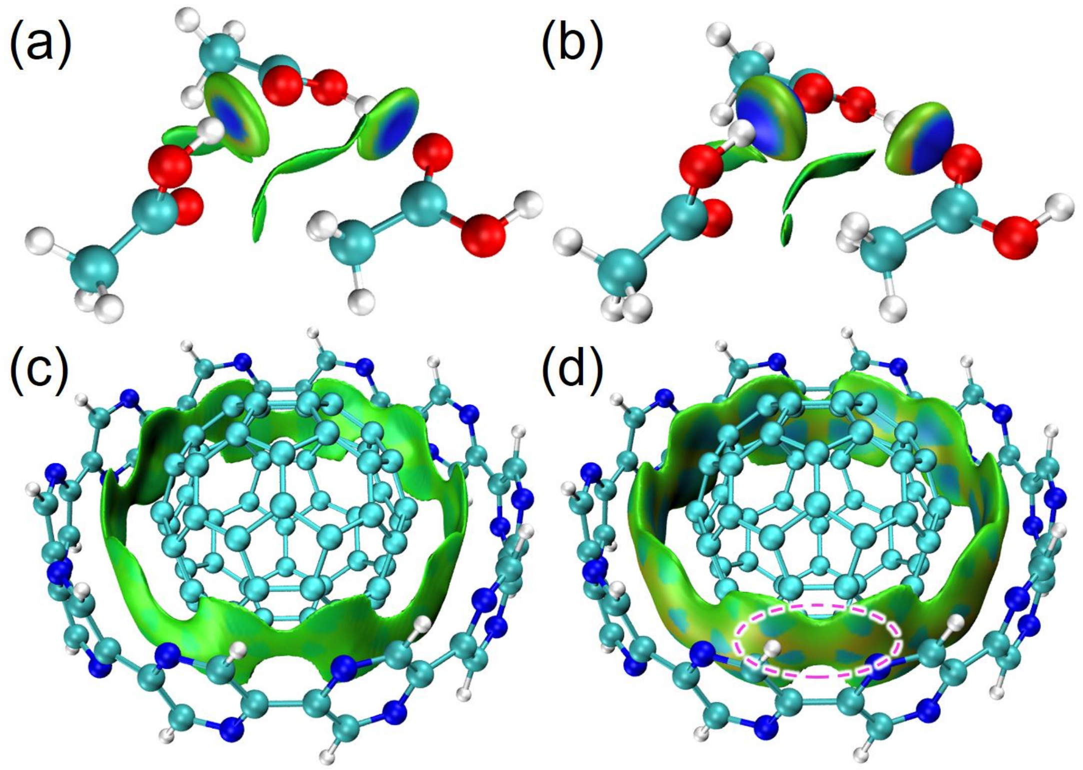

Fig. 14 (a) and (b): IGMH and IGM maps of acetic acid trimer, δg^{inter} isovalues of 0.011 and 0.006 a.u. are used respectively. $sign(\lambda_2)\rho$ is mapped on the isosurfaces according to the color bar in Fig. 2 while lower and upper limits are changed to -0.05 and 0.05 a.u., respectively. (c) and (d): IGMH and IGM maps of C_{60}:[10]CPP complex, $sign(\lambda_2)\rho$ is mapped on the isosurfaces of δg^{inter} = 0.005 a.u. according to the color bar in Fig. 2, while lower and upper limits are set to -0.04 and 0.04 a.u., respectively.

IGMH can also be successfully applied to reveal interactions in periodic systems. For example, Fig. 15(a) employs IGMH method to exhibit interactions between a chlorine molecule (defined as fragment 1) and surrounding ones (collectively defined as fragment 2) in chlorine crystal, the interactions in all directions can be viewed very clearly. Fig. 15(b) shows an adsorbed CO molecule on NaCl surface, the physical adsorption on CO due to the C···Na and C···Cl attractive interactions is well exhibited.

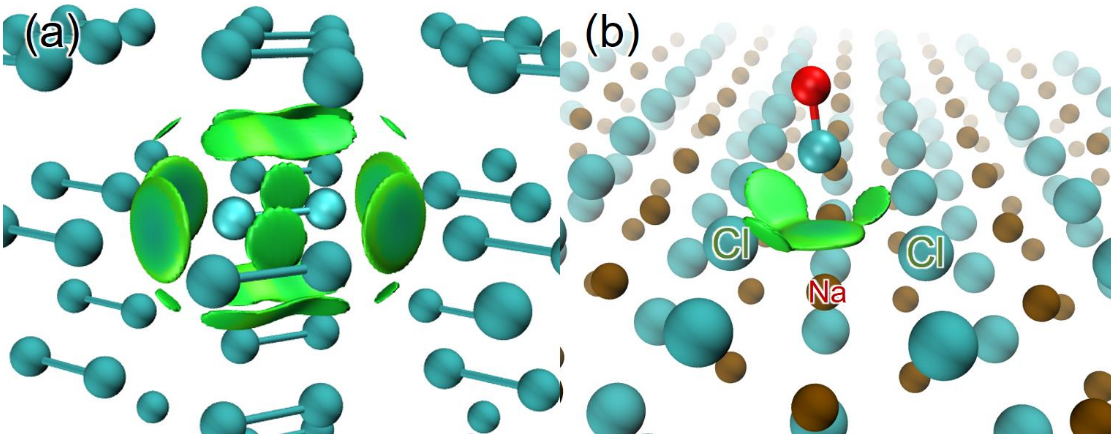

Fig. 15 IGMH map of (a) chlorine crystal and (b) adsorbed CO molecule on NaCl surface. Isovalues of 0.004 and 0.003 a.u. are employed respectively. $sign(\lambda_2)\rho$ is mapped on the isosurfaces according to Fig. 2 while color range is changed to -0.03 ~ -0.03 and -0.05 ~ 0.05 a.u. for (a) and (b), respectively.

It is worth mentioning that IGMH also has an obvious advantage over IGM in revealing chemical bond interactions. Because IGM only relies on the very rough ρ^{pro}, while the formation of chemical bonds between atoms must be accompanied by significant changes in the electronic structure in the bonding regions, therefore, description of chemical bonds by IGM is sometimes qualitatively wrong, this point has been demonstrated in Ref. [68].

Computational cost of IGMH is considerably higher than IGM, because evaluation of gradient of ρ^{Hirsh} requires value and gradient of actual ρ. The formal expense of IGMH analysis is the same as that of NCI and IRI analysis. However, it is found that IGMH map generally has a lower requirement on grid quality; in other words, when grid quality is not very fine, isosurfaces in IGMH map are evidently smoother and less jaggy than NCI and IRI maps. Therefore, using a relatively large grid spacing (*e.g.* 0.2 Bohr or even larger) for saving computational cost in IGMH analysis is usually tolerable.

Compared with IGM, IGMH has notably better results and stronger physical meaning. So, we always recommend using IGMH instead of IGM when the system is not particularly large and hence too difficult to carry out DFT calculations.

It is worth noting that there is another variant of IGM based on actual electronic structure, which was proposed by Hénon et al.[74] and will be referred to as IGM(GBP). Unlike IGMH, which only involves partition of ρ, the IGM(GBP) method employs the so-called gradient-based partitioning technique, which explicitly involves orbital wavefunctions. The principle of IGM(GBP) is significantly more abstract and complicated than the original IGM method, and its realization is currently only limited to closed-shell single-determinant wavefunction. IGM(GBP) does not seem to have obvious advantages over IGM in showing weak interactions, while its authors believed that IGM(GBP) works more reasonably for studying chemical bond interactions.

6 aNCI and aIGM methods: Analysis for fluctuation environment

NCI analysis only gives visual representation of weak interactions for a single structure, however, in reality, molecules are always in dynamic environment. Especially in condensed phase or in a complex, because the surrounding atoms or molecules are constantly in motion, the interaction between the molecule under investigation and the external environment is constantly changing. Evidently, it is of great importance to devise a NCI-like method with explicit consideration of dynamic environment to faithfully reveal weak interactions in real situations. Based on this idea, Yang et al. extended the original NCI method and defined averaged NCI (aNCI) method.[75] Commonly aNCI is applied to the trajectory frames generated by MD simulation.

The main difference between aNCI and the original NCI method is that in the former, ρ and its gradient norm are not calculated for only one geometry, but for multiple frames in a trajectory file. Specifically, aNCI defines averaged RDG (aRDG) as

$$\mathrm{aRDG}(\mathbf{r}) = \frac{1}{2(3\pi^2)^{1/3}} \frac{|\overline{\nabla\rho}(\mathbf{r})|}{\left[\bar{\rho}(\mathbf{r})\right]^{4/3}} \tag{18}$$

where $\bar{\rho}$ and $\overline{\nabla\rho}$ stand for averaged ρ and $\nabla\rho$ for considered trajectory frames, respectively. The averaged weak interactions during MD simulation are graphically exhibited in terms of isosurfaces of aRDG. In order to distinguish the type of weak interactions, the aNCI method utilizes averaged $sign(\lambda_2)\rho$ function, in which ρ corresponds to $\bar{\rho}$, and λ_2 is calculated as the second largest eigenvalue of the averaged electron density Hessian matrix computed throughout the dynamical trajectory.

aNCI method also defines a function named thermal fluctuation index (TFI) to reveal stability of weak interactions.

$$\mathrm{TFI}(\mathbf{r}) = \frac{std[\rho(\mathbf{r})]}{\bar{\rho}(\mathbf{r})} \tag{19}$$

whose numerator is standard deviation of ρ in the dynamical trajectory, which is expressed as

$$std[\rho(\mathbf{r})] = \sqrt{\frac{\sum_i [\rho_i(\mathbf{r}) - \bar{\rho}(\mathbf{r})]^2}{n}} \tag{20}$$

where n is the number of frames in consideration, ρ_i denotes the electron density calculated for frame i. The idea of definition of TFI is easy to comprehend: standard deviation of ρ is a direct metric of fluctuation of ρ, if at a point this quantity is large with respect to $\bar{\rho}$, then the weak interaction in this place must have a low stability. After mapping TFI on the isosurfaces of aRDG, the thermal stability of every weak interaction region can be identified by visually examining the colors.

All visualization methods introduced in previous sections do not have the capability to directly reveal how temperature and external pressure affect occurrence region and strength of weak interactions. In this regard, aNCI method has a unique value. In MD simulation, both temperature and external pressure can be set by researchers according to practical requirement, so aNCI analysis is able to characterize the weak interactions at specific condition. Obviously, aNCI method can also be used to study how weak interaction characteristics change with variation of external conditions, such as annealing process.

Since aNCI analysis usually calculates at least a few hundreds of structures, in principle its time-consuming is at least two orders of magnitude higher than that of NCI analysis, so aNCI analysis based on actual electron density is generally computationally infeasible. In order to maximally reduce calculation cost, in the original paper of the aNCI method and in the aNCI module of Multiwfn program, the aNCI analysis is conducted based on promolecular approximation.

Fig. 16 is aNCI map of phenol in water environment, this example fully illustrates the importance of aNCI map in understanding weak interactions in condensed phase. The MD simulation was conducted via GROMACS program[76] by us at 298.15 K and 1 atm, the phenol and waters were represented by GAFF forcefield[77] and SPC/E model, respectively. The phenol was fixed at center of a water box. The trajectory frames were saved every 1 ps and totally 1000 frames were taken into account in the aNCI analysis. Fig. 16(a) shows averaged $sign(\lambda_2)\rho$ colored aRDG isosurfaces, from the dark blue isosurface close to the hydrogen of the hydroxyl group one can recognize that a H-bond between the phenol (H-bond donor) and environment waters (H-bond acceptors) during MD simulation almost always occurs at this site, and this inference can be verified via visual inspection of the structures in the MD trajectory. The oxygen of the hydroxyl group can act as an acceptor of the H-bond with water in the MD simulation, as there is a light blue color on the corresponding region of the aRDG isosurface. The flat isosurfaces above and below the aromatic ring of phenol show cyan color, implying that the ring forms prominent O-H$\cdots\pi$ type of H-bond interaction with waters. In Fig. 16(a) there is also a very broad green isosurface around the phenol, which well exhibits the averaged vdW interactions between the phenol and environment molecules. Note that NCI^{pro} is equivalent to the case that only one frame is considered in aNCI analysis. If NCI^{pro} map is plotted, it will be found that the isosurfaces showing the phenol-water vdW interactions are completely discretely distributed, therefore the aNCI method has to be employed if one intends to study averaged vdW interactions. Fig. 16(b) shows the aRDG isosurfaces colored by TFI, in which blue, green and red colors correspond to small, medium and high TFI values, respectively. From the color it can be seen that the O-H$\cdots$O H-bond between the phenol (H-bond donor) and environment waters has a good stability, while the O-H$\cdots\pi$ H-bond only has a modest stability mostly because its interaction strength is evidently lower than the O-H···O H-bond. The vdW interaction regions around the phenol show highest TFI and thus poorest stability, indicating that the interactions in these areas are constantly changing. Some readers may find that the colors of the inside and outside of the isosurfaces in Fig. 16(b) are somewhat different, this is because the isosurfaces have a certain thickness. In our opinion, the color outside the isosurfaces should be focused on, because these areas are farther from nuclei, where the TFI can better capture the stability characteristics of weak interactions between solute and environment molecules.

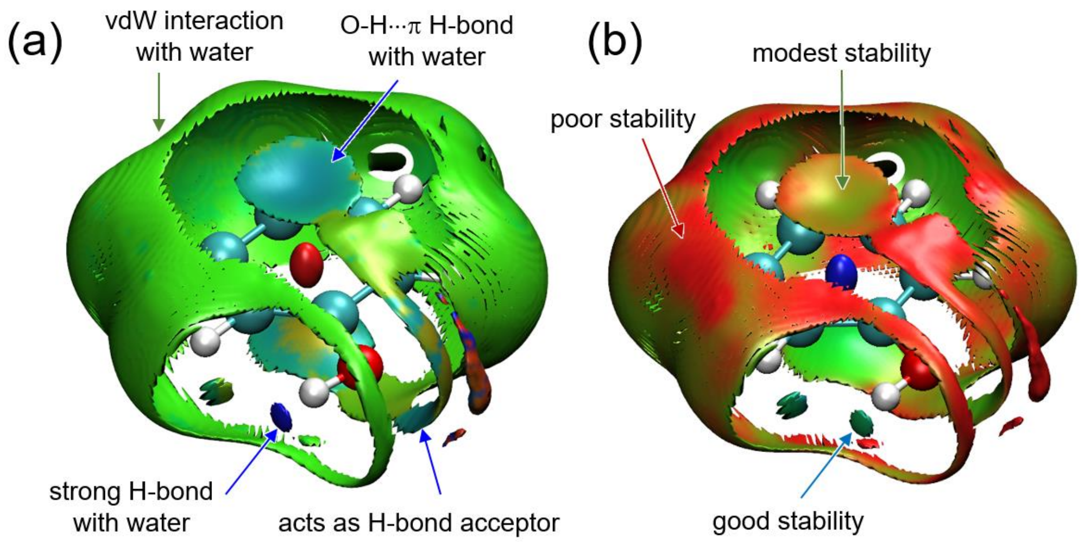

Fig. 16 aNCI map of phenol in water environment. (a) Averaged $sign(\lambda_2)\rho$ colored aRDG = 0.25 isosurfaces, the coloring method is the same as Fig. 2 while lower and upper limits are changed to -0.025 and 0.025 a.u., respectively (b) TFI colored aRDG isosurfaces, blue, green and red correspond to small, medium and high TFI values, respectively.

aNCI is also quite valuable in studying protein-ligand interaction in real environment. As an example, Fig. 17 presents aNCI map showing interaction between benzamidine ligand and surrounding amino acid residues in trypsin protein. The frames used in the aNCI analysis were evenly extracted from MD simulation at 298.15 K for 1 ns under explicit water box. From the averaged $sign(\lambda_2)\rho$ colored aRDG isosurfaces in Fig. 17(a), the broad range vdW interactions and the four prominent H-bonds between the ligand and protein can be intuitively observed. In Fig. 17(b), the colors corresponding to TFI indicate that the four H-bonds form stably during simulation. Although vdW interaction is by far weaker than common H-bond, since the benzamidine ligand is in a less fluctuated protein local environment, some protein-ligand vdW interactions also exist stably, as shown by the blue color in corresponding isosurfaces. However, the green color in this map shows that there are also vdW interactions with relatively weak stability.

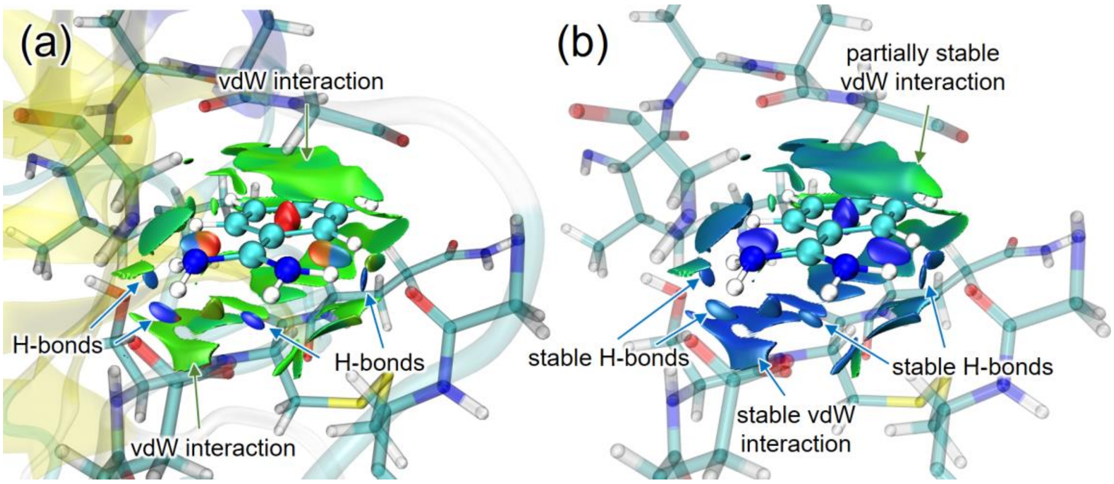

Fig. 17 aNCI map showing benzamidine (ball and stick style) and the amino acid residues in trypsin closely contacted to it (stick style) in protein-ligand complex (PDB ID: 3ATL). (a) Averaged $sign(\lambda_2)\rho$ colored aRDG = 0.3 isosurfaces, the coloring method is the same as Fig. 2 while lower and upper limits are changed to -0.04 and 0.04 a.u., respectively. Backbone of the protein is drawn as new cartoon style. (b) TFI colored aRDG isosurfaces, blue, green and red correspond to small, medium and high TFI values, respectively.

The averaged independent gradient model (aIGM) proposed by us[78] is an extension of IGM analysis to dynamic environment. The relationship between aIGM and IGM is similar with that between aNCI and NCI. aIGM is very suitable for studying averaged interactions between two or more specific fragments during MD simulation. aIGM defines a function $\delta\bar{g}^{\mathrm{inter}}$, which measures averaged interaction between user-defined fragments

$$\delta \bar{g}^{\text{inter}}(\mathbf{r}) = \bar{g}^{\text{IGM,inter}}(\mathbf{r}) - \bar{g}^{\text{inter}}(\mathbf{r}) \tag{21}$$

where

$$\begin{aligned} \bar{g}^{\text{inter}}(\mathbf{r}) &= \left| \sum_{A} \left\langle \sum_{i \in A} \nabla \rho_i^{\text{free}}(\mathbf{r}) \right\rangle \right| \\ \bar{g}^{\text{IGM,inter}}(\mathbf{r}) &= \sum_{A} \left| \left\langle \sum_{i \in A} \nabla \rho_i^{\text{free}}(\mathbf{r}) \right\rangle \right| \end{aligned} \tag{22}$$

in which i is atomic index, A is fragment index, and the angle brackets stand for time average for all considered trajectory frames. Like aNCI map, in aIGM map averaged $sign(\lambda_2)\rho$ is mapped on $\delta\bar{g}^{\text{inter}}$ isosurfaces to distinguish interaction types. The aIGM method has recently been implemented in our Multiwfn program, and we plan to conduct a comprehensive investigation on its characteristics in the future.

According to our experiences, the following points need to be paid attention when performing aNCI or aIGM analysis:

(1) If it is expected that the position of the molecule under investigation will spontaneously change during MD simulation process, the molecule should be frozen or be restrained by external potentials to keep its position fixed during the simulation, otherwise distribution of the generated isosurfaces will be very messy and useless.

(2) If the molecule under investigation has an obvious flexibility and thus the conformation changes repeatedly during the MD simulation, aNCI or aIGM analysis should not be carried out directly on the entire trajectory, otherwise the resulting map will be very confusing. In this case, we suggest performing cluster analysis for the trajectory to obtain dominant conformations of the molecule, and then the aNCI or aIGM analysis should be conducted respectively for the trajectory ranges corresponding to the different dominant conformations, then from the resulting maps one will be able to understand the difference of weak interactions corresponding to the molecule in different conformations.

(3) Normally, the molecule under investigation should always be in the center of the simulation box and explicitly surrounded by environmental molecules, so that its interaction with external environment can be faithfully displayed by aNCI or aIGM map.

(4) The quality of aNCI map highly depends on the number of frames that taken into account. Small number of frames, for example 50, usually leads to inaccurate and very non-smooth aRDG isosurfaces. In general, at least 500 frames should be used to generate a satisfactory aNCI map. Quality of aIGM map has notably lower requirement on the number of considered frames.

7 Comparison of various visualization methods

To facilitate readers to understand the differences between various visualization analysis methods described above, a comparison is presented in Table 2.

Table 2 Comparison of various visualization analysis methods

	NCI	NCI^{pro}	DORI / IRI	IGM	IGM(GBP)	IGMH
Revealing weak interactions	Y	Y	Y	Y	Y	Y
Revealing strong interactions	N	N	Y	Y^{a}	Y^{a}	Y^{a}
Partitioning fragments	N	N	N	Y	Y	Y
Needed information	ρ	ρ^{pro}	ρ	ρ^{pro}	wavefunction	ρ
Sensitivity to grid quality	high	high	high	low	low	medium
Cost	medium	low	medium	very low	medium	medium
Variant for dynamic environment	none	aNCI	none	aIGM	none	none

^{a} Depending on isovalue

Our recommendation for the use of different methods in various situations is given below.

NCI: Suitable for visually revealing all weak interactions in a system.

NCI^{pro}: Suitable as the low-cost substitute for NCI method when the system to be studied is huge, or requirement on the result quality is low.

IRI: Well-suited for revealing all kinds of interactions in a system, and visually monitoring transition of bonding in a chemical reaction process.

IGMH: Suitable for individually revealing intrafragment and interfragment interactions, as well as quantifying and visually representing atomic and atomic pair contributions.

IGM: Suitable as the low-cost substitute for IGMH when the system to be studied is too large to conduct a quantum chemistry calculation and IGMH analysis.

aNCI: When the weak interaction to be studied is noticeably affected by the actual dynamic environment, or the influence of external conditions on weak interactions needs to be investigated, aNCI should be used instead of NCI.

aIGM: Suitable to be used instead of aNCI when weak interaction between specific molecules is of interest and needed to be studied individually.

Regarding the computational cost, in the efficient and highly parallelized Multiwfn code, for the current mainstream calculation conditions (a computing server with dozens of CPU cores), NCI, IRI and IGMH analyses can be realized for a system containing hundreds of atoms without any difficulty (assumed that the system is a typical organic system and a medium-sized basis set is used). While for IGM and NCI^{pro} analyses, they can even be easily performed for systems containing as many as thousands of atoms. Note that the actual time consuming is highly dependent of grid spacing and spatial range of grid data. By properly defining grid data range, significant computational cost may be saved. When consideration of periodic boundary condition is requested in Multiwfn code, the cost will be increased by several times since atoms in adjacent image cells will be looped over.

8 Programs of realizing visualization analyses

All currently available computer programs that support the methods introduced in this chapter are collected in Table 3. As can be recognized from the table, the Multiwfn program developed by us is powerful in visual analysis of interactions, therefore it will be briefly described below. Note that Multiwfn is always in rapid development, the following content corresponds to version 3.8 released in 2021.

Table 3 Summary of computer codes for visual analysis of interactions in chemical systems.

	Multiwfn	NCIplot	IGMplot	Critic2	NCImilano	AIMALL

Methods related to visual analysis	NCI, NCI^{pro}, aNCI, IRI, DORI, IGM, IGMH, aIGM, AIM, ESP, V^{vdw}, ETS-NOCV, EDA-FF, Hirshfeld surface, etc.	NCI, NCI^{pro}	NCI, IGM, IGM(GBP)	NCI, NCI^{pro}, AIM	NCI, NCI^{pro}	AIM, NCI, etc.
Availability	free+open	free+open	free+open	free+open	free	free / charge[a]
Periodicity	Y[b]	N	N	Y	Y	N
Quantification[b]	Y	Y	Y	N	N	N
Parallelization	Y (OpenMP)	Y (OpenMP)	Y (OpenMP)	Y (OpenMP)	N	Yes
Input file formats	wfn, wfx, mwfn, fch, molden, xyz, pdb, mol2, cif, cub, etc.	xyz, wfn, wfx	xyz, wfn, wfx	wfn, wfx, fch, molden, xyz, cif, cub, etc.	wfn, cub, grd	wfn, wfx, fch
Interface	interactive text with GUI, or command-line	command-line	command-line	command-line	command-line	GUI or command-line
Language	Fortran	Fortran	C++	Fortran	Unknown	Unknown
Latest version	3.8	4.0	2.6.9b	1.1	1.0	19.10.12

[a] Standard version is free of charge, but has evident limitation on parallel running and visualization.

[b] One-, two-, three-dimensional periodicities are supported and can be chosen by user.

[c] NCI integration is supported by Multiwfn and NCIplot, evaluation of δG^{atom}, δG^{pair} and δG^{inter} is supported by Multiwfn and IGMplot.

Basic features

Multiwfn[24] is an ease-to-use, efficient, flexible and highly integrated wavefunction analysis code, supporting almost all of the most important wavefunction methods. Its precompiled executable file for all platforms (Windows, Linux, MacOS), source code, manual, tutorial and various related documents, can be directly and freely downloaded at its official website. Multiwfn is popular in the field of electronic wavefunction analysis. Since its first formal release in 2011, more than 8000 scientific papers using Multiwfn to perform various kinds of analysis have been published.

Except for IGM(GBP), all methods introduced in this chapter can be realized via Multiwfn. In addition, as shown in Table 3, Multiwfn also supports many other methods of graphical analysis of interactions in chemical systems: electrostatic potential (ESP) analysis is very useful in intuitively understanding intermolecular electrostatic interaction;[79] vdW potential (V^{vdw}) is an important function for visually predicting and interpreting vdW interaction strength between external substances and various regions of the present system;[80] electron density difference ($\nabla\rho$) plotted by Multiwfn is able to graphically exhibit variation of ρ due to interaction between specific fragments;[9, 81] extended transition state - natural orbitals for chemical valence (ETS-NOCV) analysis is capable of decomposing $\nabla\rho$ into contributions from different kinds of interactions with corresponding interaction energies;[82] contributions of atoms to interfragment interaction energy can be estimated by energy decomposition analysis based on forcefield (EDA-FF) method and mapped on atoms by different colors to vividly exhibit the role played by various atoms;[83] Hirshfeld surface analysis is able to characterize interaction between a molecule and surrounding ones in molecular crystals via molecular surface map colored by special functions.[84]

The use of Multiwfn is fair convenient, the program design allows users to complete various analyses with as few steps as possible. Multiwfn has a text-based user-friendly interactive interface, users do not need to memorize any keyword and manually write input files, they simply need to input commands by following the prompts on the screen. It is also noteworthy that one can easily run Multiwfn purely via command-line, and embed the code into shell script to perform analysis for a large number of systems, such as realizing IRI analysis for all structures in an IRC trajectory.

Multiwfn has a quite detailed manual with more than 1000 pages to facilitate users to use, which not only carefully introduces theory background, implementation and usage of various analysis methods available in Multiwfn, but also provides a very systematic tutorial containing numerous examples. The realization of any visual analysis method introduced in this chapter can be easily learned within a few minutes by following corresponding examples in the manual.

Input file

Multiwfn accepts input file in wide variety of formats for the aforementioned visual analyses:

(1) NCI, DORI, IRI, and IGMH analyses for isolated systems: Any file format

containing electronic wavefunction information can be used, such as mwfn,[85] wfn, wfx, fch, molden, GAMESS/Firefly output file, and so on. Basically all popular quantum chemistry programs are able to export at least one of them, and the exporting methods have been carefully documented in Multiwfn manual.

(2) NCI, DORI, IRI, and IGMH analyses for periodic systems: The input file should contain both periodic wavefunction and cell information. Molden file exported by CP2K first-principle program[86] after DFT calculation is usually used in this context, cell vectors should be manually filled into it, see Multiwfn manual for details. mwfn[85] and fch files containing cell vectors are also supported for this purpose. Note that *k*-point sampling is currently not supported, so users should employ a large enough cell to conduct the DFT calculation in CP2K and visual analysis in Multiwfn.

(3) NCI^{pro} and IGM analyses for isolated systems: Any file format containing atomic coordinates can be used, such as xyz, mol, mol2, pdb, input/output file of Gaussian and ORCA programs, and so on.

(4) NCI^{pro} and IGM analysis for periodic systems: The input file should contain both atomic coordinates and cell information. For example, cif, cub, gro file of GROMACS program, restart file of CP2K program, POSCAR file of VASP program, Gaussian input file containing cell vectors.

(5) aNCI and aIGM analyses: xyz trajectory file containing MD frames should be used.

It is noteworthy that using Multiwfn to visual study interactions of excited state is also possible, as long as the input file contains excited state wavefunction. Multiwfn loads wavefunction from input file in terms of orbitals, therefore if the excited state is evaluated by a multiconfiguration method, such as time-dependent DFT (TDDFT) and EOM-CCSD, natural orbitals of the excited state of interest should be recorded in the input file.

Basic steps of plotting NCI map

In order to provide readers with a clear impression on how to easily obtain the very valuable NCI map using Multiwfn in combination with VMD, here we provide a very brief illustration, detailed descriptions and discussions can be found in manual. Other NCI-related analysis can be realized in a very similar way. The VMD visualization software[25] can be freely obtained at its website. It is assumed that the reader is using Multiwfn 3.8 and VMD 1.9.3.

The first step is to optimize geometry and meantime generate wavefunction file. For the popular Gaussian quantum chemistry program, a template input file is given below, the [geometry] should be replaced with actual initial geometry.

```
# wB97XD/6-311G** opt out=wfn

Geometry optimization

0 1
[geometry]

D:\opted.wfn
```

After calculation, "opted.wfn" will be generated in D:\ directory, which contains wavefunction at optimized geometry.

Then boot up Multiwfn and input the following commands. The texts after double slash are comments.

D:\opted.wfn

20 // Visual analysis of weak interactions

1 // NCI analysis

4 // Defining grid via mode 4. In this case grid spacing is directly set by user, and grid points cover the entire system.

0.15 // Grid spacing

After calculation, a post-process menu appears on screen. Select corresponding option to export "func1.cub" and "func2.cub", which record grid data of $sign(\lambda_2)\rho$ and RDG, respectively.

Then manually move the two cube files and the VMD plotting script "RDGfill.vmd" in Multiwfn package to VMD installation folder. Boot up VMD and input *source RDGfill.vmd* in VMD console window to execute the script, then $sign(\lambda_2)\rho$

colored RDG isosurface map will be immediately shown on graphical window. The default isovalue and color scale can be further adjusted in VMD in “Graphics” - “Representation” panel.

9 Summary

Since the NCI method was proposed in 2010, visual analysis on weak interactions has rapidly become popular in the field of chemistry. This chapter introduces NCI and various related methods proposed later, including IRI, DORI, IGM, IGMH, and so on. This chapter not only comprehensively introduces the basic ideas and theoretical backgrounds of these methods, but also compares their difference, and meantime some our personal views and suggestions about realizing the analyses are given. The large number of application examples of the above methods in this chapter involve wide variety of chemical systems and various forms of weak interactions, they fully demonstrate the significant and irreplaceable value of the visual analysis methods. From the examples it can be seen that these methods are able to reveal occurrence regions of important weak interactions and distinguish their types in a very intuitive way, so that chemists can easily and quickly understand characteristics of weak interactions in a system. In addition, some methods can also provide indices related to strength of weak interactions and contributions from atoms or atom pairs, which are very convenient for researchers to investigate weak interactions quantitatively. In addition, this chapter also lists all existing softwares that can realize the visual analysis of weak interactions, and provides a brief introduction to Multiwfn, which is a wavefunction analysis code rich in functions, efficient, and easy-to-use even for quantum chemistry beginners. We hope that this chapter will enable readers to have a comprehensive understanding of the visual analysis methods of weak interactions and apply it to the study of a wide range of practical problems.

List of relevant websites

Multiwfn website: http://sobereva.com/multiwfn

VMD website: http://www.ks.uiuc.edu/Research/vmd/

IGMplot website: http://igmplot.univ-reims.fr/

NCIplot website: https://www.lct.jussieu.fr/pagesperso/contrera/index-nci.html

Critic 2 website: https://aoterodelaroza.github.io/critic2/

NCImilano website: https://www.lct.jussieu.fr/pagesperso/contrera/nci-milano.html

Gaussian website: http://www.gaussian.com/

CP2K website: https://www.cp2k.org

References

1. S. Emamian; T. Lu; H. Kruse; H. Emamian. Exploring Nature and Predicting Strength of Hydrogen Bonds: A Correlation Analysis Between Atoms-in-Molecules Descriptors, Binding Energies, and Energy Components of Symmetry-Adapted Perturbation Theory. *J. Comput. Chem.*, **40**, 2868-2881 (2019). DOI: 10.1002/jcc.26068.
2. E. Arunan; G. R. Desiraju; R. A. Klein; J. Sadlej; S. Scheiner; I. Alkorta; D. C. Clary; R. H. Crabtree; J. J. Dannenberg; P. Hobza; H. G. Kjaergaard; A. C. Legon; B. Mennucci; D. J. Nesbitt. Definition of the hydrogen bond (IUPAC Recommendations 2011). *Pure Appl. Chem.*, **83**, 1637-1641 (2011). DOI: 10.1351/PAC-REC-10-01-02.
3. G. Cavallo; P. Metrangolo; R. Milani; T. Pilati; A. Priimagi; G. Resnati; G. Terraneo. The Halogen Bond. *Chem. Rev.*, **116**, 2478-2601 (2016). DOI: 10.1021/acs.chemrev.5b00484.
4. P. Politzer; J. S. Murray; T. Clark. Halogen bonding: an electrostatically-driven highly directional noncovalent interaction. *Phys. Chem. Chem. Phys.*, **12**, 7748-7757 (2010). DOI: 10.1039/C004189K.
5. Q. Yang; Y. Liu; Z. Zhang; F. Zhou; Z. Wang; B. Zheng; T. Lu. Probing the halogen bond donation ability of multivalent At-center in AtXn (X = Cl, Br, I; n = 1, 3, 5)···H2O/H2S complexes. *Comput. Theor. Chem.*, **1195**, 113090 (2021). DOI: 10.1016/j.comptc.2020.113090.
6. F. Zhou; Y. Liu; Z. Wang; T. Lu; Q. Yang; Y. Liu; B. Zheng. A new type of halogen bond involving multivalent astatine: an ab initio study. *Phys. Chem. Chem. Phys.*, **21**, 15310-15318 (2019). DOI: 10.1039/C9CP02406A.
7. V. Oliveira; D. Cremer; E. Kraka. The Many Facets of Chalcogen Bonding: Described by Vibrational Spectroscopy. *J. Phys. Chem. A*, **121**, 6845-6862 (2017). DOI: 10.1021/acs.jpca.7b06479.
8. Y. Jiao; Y. Liu; W. Zhao; Z. Wang; X. Ding; H. Liu; T. Lu. Theoretical study on the interactions of halogen-bonds and pnicogen-bonds in phosphine derivatives with Br2, BrCl, and BrF. *Int. J. Quantum Chem.*, **117**, e25443 (2017). DOI: 10.1002/qua.25443.
9. Z. Zhang; T. Lu; L. Ding; G. Wang; Z. Wang; B. Zheng; Y. Liu; X. L. Ding. Cooperativity effects

between regium-bonding and pnicogen-bonding interactions in ternary MF···PH3O···MF (M = Cu, Ag, Au): an ab initio study. *Mol. Phys.*, **118**, e1784478 (2020). DOI: 10.1080/00268976.2020.1784478.
10. D. J. Wolstenholme; T. S. Cameron. Comparative Study of Weak Interactions in Molecular Crystals: H−H Bonds vs Hydrogen Bonds. *J. Phys. Chem. A*, **110**, 8970-8978 (2006). DOI: 10.1021/jp061205i.
11. B. Jeziorski; R. Moszynski; K. Szalewicz. Perturbation Theory Approach to Intermolecular Potential Energy Surfaces of van der Waals Complexes. *Chem. Rev.*, **94**, 1887-1930 (1994). DOI: 10.1021/cr00031a008.
12. Z. Liu; T. Lu; Q. Chen. Intermolecular interaction characteristics of the all-carboatomic ring, cyclo[18]carbon: Focusing on molecular adsorption and stacking. *Carbon*, **171**, 514-523 (2021). DOI: 10.1016/j.carbon.2020.09.048.
13. S. Grimme. Do Special Noncovalent π–π Stacking Interactions Really Exist? *Angew. Chem. Int. Ed.*, **47**, 3430-3434 (2008). DOI: 10.1002/anie.200705157.
14. J. P. Wagner; P. R. Schreiner. London Dispersion in Molecular Chemistry—Reconsidering Steric Effects. *Angew. Chem. Int. Ed.*, **54**, 12274-12296 (2015). DOI: 10.1002/anie.201503476.
15. P. Lipkowski; S. J. Grabowski; T. L. Robinson; J. Leszczynski. Properties of the C−H···H Dihydrogen Bond: An ab Initio and Topological Analysis. *J. Phys. Chem. A*, **108**, 10865-10872 (2004). DOI: 10.1021/jp048562i.
16. F. W. Bader. *Atoms in Molecules: A Quantum Theory*. Oxford University Press: New York (1994).
17. C. F. Matta; R. J. Boyd, Eds. *The Quantum Theory of Atoms in Molecules - From Solid State to DNA and Drug Design*. WILEY-VCH Verlag GmbH & Co. KGaA: Weinheim (2007).
18. M. J. L. Mills; K. L. Sale; B. A. Simmons; P. L. A. Popelier. Rhorix: An interface between quantum chemical topology and the 3D graphics program blender. *J. Comput. Chem.*, **38**, 2538-2552 (2017). DOI: 10.1002/jcc.25054.
19. F. Weinhold. Natural Bond Orbital Methods. In *Encyclopedia of Computational Chemistry*, P. v. R. Schleyer, Ed. John Wiley & Sons: West Sussex (1998); Vol. 2, pp 1792-1811.
20. E. D. Glendening; C. R. Landis; F. Weinhold. Natural bond orbital methods. *WIREs Comput. Mol. Sci.*, **2**, 1-42 (2012). DOI: 10.1002/wcms.51.
21. M. J. S. Phipps; T. Fox; C. S. Tautermann; C.-K. Skylaris. Energy decomposition analysis approaches and their evaluation on prototypical protein–drug interaction patterns. *Chem. Soc. Rev.*, **44**, 3177-3211 (2015). DOI: 10.1039/C4CS00375F.
22. E. Pastorczak; C. Corminboeuf. Perspective: Found in translation: Quantum chemical tools for grasping non-covalent interactions. *J. Chem. Phys.*, **146**, 120901 (2017). DOI: 10.1063/1.4978951.
23. E. R. Johnson; S. Keinan; P. Mori-Sánchez; J. Contreras-García; A. J. Cohen; W. Yang. Revealing Noncovalent Interactions. *J. Am. Chem. Soc.*, **132**, 6498-6506 (2010). DOI: 10.1021/ja100936w.
24. T. Lu; F. Chen. Multiwfn: A Multifunctional Wavefunction Analyzer. *J. Comput. Chem.*, **33**, 580-592 (2012). DOI: 10.1002/jcc.22885.
25. W. Humphrey; A. Dalke; K. Schulten. VMD: Visual molecular dynamics. *J. Mol. Graph.*, **14**, 33-38 (1996). DOI: 10.1016/0263-7855(96)00018-5.
26. T. Lu; S. Manzetti. Wavefunction and reactivity study of benzo[a]pyrene diol epoxide and its enantiomeric forms. *Struct. Chem.*, **25**, 1521-1533 (2014). DOI: 10.1007/s11224-014-0430-6.
27. S. Manzetti; T. Lu. The geometry and electronic structure of Aristolochic acid: possible implications for a frozen resonance. *J. Phys. Org. Chem.*, **26**, 473-483 (2013). DOI: 10.1002/poc.3111.
28. I. González-Veloso; J. A. Carrazana-García; D. Josa; J. Rodríguez-Otero; E. M. Cabaleiro-Lago.

NCI analysis of the interaction cation···π in complexes with molecular bowls derived from fullerene. *Comput. Theor. Chem.*, **1053**, 123-129 (2015). DOI: 10.1016/j.comptc.2014.10.012.
29. J. Contreras-García; E. R. Johnson; S. Keinan; R. Chaudret; J.-P. Piquemal; D. N. Beratan; W. Yang. NCIPLOT: A Program for Plotting Noncovalent Interaction Regions. *J. Chem. Theory Comput.*, **7**, 625-632 (2011). DOI: 10.1021/ct100641a.
30. F. Adasme-Carreño; J. Alzate-Morales; J. Ireta. Modeling cooperative effects in halogen-bonded infinite linear chains. *Phys. Chem. Chem. Phys.*, **19**, 18529-18538 (2017). DOI: 10.1039/C7CP03078A.
31. Z. Liu; T. Lu; Q. Chen. An sp-hybridized all-carboatomic ring, cyclo[18]carbon: Electronic structure, electronic spectrum, and optical nonlinearity. *Carbon*, **165**, 461-467 (2020). DOI: 10.1016/j.carbon.2020.05.023.
32. Z. Liu; T. Lu; Q. Chen. An sp-hybridized all-carboatomic ring, cyclo[18]carbon: Bonding character, electron delocalization, and aromaticity. *Carbon*, **165**, 468-475 (2020). DOI: 10.1016/j.carbon.2020.04.099.
33. N. O. B. Lüttschwager; T. N. Wassermann; R. A. Mata; M. A. Suhm. The Last Globally Stable Extended Alkane. *Angew. Chem. Int. Ed.*, **52**, 463-466 (2013). DOI: 10.1002/anie.201202894.
34. S. Ehrlich; H. F. Bettinger; S. Grimme. Dispersion-Driven Conformational Isomerism in σ-Bonded Dimers of Larger Acenes. *Angew. Chem. Int. Ed.*, **52**, 10892-10895 (2013). DOI: 10.1002/anie.201304674.
35. A. Otero-de-la-Roza; E. R. Johnson; V. Luaña. Critic2: A program for real-space analysis of quantum chemical interactions in solids. *Comput. Phys. Commun.*, **185**, 1007-1018 (2014). DOI: 10.1016/j.cpc.2013.10.026.
36. J. R. Lane; J. Contreras-García; J.-P. Piquemal; B. J. Miller; H. G. Kjaergaard. Are Bond Critical Points Really Critical for Hydrogen Bonding? *J. Chem. Theory Comput.*, **9**, 3263-3266 (2013). DOI: 10.1021/ct400420r.
37. T. Lu; Q. Chen. Interaction Region Indicator: A Simple Real Space Function Clearly Revealing Both Chemical Bonds and Weak Interactions. *Chemistry-Methods*, **1**, 231-239 (2021). DOI: 10.1002/cmtd.202100007.
38. J. Contreras-García; W. Yang; E. R. Johnson. Analysis of Hydrogen-Bond Interaction Potentials from the Electron Density: Integration of Noncovalent Interaction Regions. *J. Phys. Chem. A*, **115**, 12983-12990 (2011). DOI: 10.1021/jp204278k.
39. F. Peccati. NCIPLOT4 Guide for Biomolecules: An Analysis Tool for Noncovalent Interactions. *J. Chem. Inf. Model.*, **60**, 6-10 (2020). DOI: 10.1021/acs.jcim.9b00950.
40. R. A. Boto; F. Peccati; R. Laplaza; C. Quan; A. Carbone; J.-P. Piquemal; Y. Maday; J. Contreras-García. NCIPLOT4: Fast, Robust, and Quantitative Analysis of Noncovalent Interactions. *J. Chem. Theory Comput.*, **16**, 4150-4158 (2020). DOI: 10.1021/acs.jctc.0c00063.
41. J. Contreras-García; R. A. Boto; F. Izquierdo-Ruiz; I. Reva; T. Woller; M. Alonso. A benchmark for the non-covalent interaction (NCI) index or… is it really all in the geometry? *Theor. Chem. Acc.*, **135**, 242 (2016). DOI: 10.1007/s00214-016-1977-7.
42. D. Arias-Olivares; E. K. Wieduwilt; J. Contreras-García; A. Genoni. NCI-ELMO: A New Method To Quickly and Accurately Detect Noncovalent Interactions in Biosystems. *J. Chem. Theory Comput.*, **15**, 6456-6470 (2019). DOI: 10.1021/acs.jctc.9b00658.
43. F. Himo. Recent Trends in Quantum Chemical Modeling of Enzymatic Reactions. *J. Am. Chem. Soc.*, **139**, 6780-6786 (2017). DOI: 10.1021/jacs.7b02671.
44. A. Kovács; J. Cz. Dobrowolski; S. Ostrowski; J. E. Rode. Benchmarking density functionals in

conjunction with Grimme's dispersion correction for noble gas dimers (Ne2, Ar2, Kr2, Xe2, Rn2). *Int. J. Quantum Chem.*, **117**, e25358 (2017). DOI: 10.1002/qua.25358.
45. E. K. Wieduwilt; G. Macetti; A. Genoni. Climbing Jacob's Ladder of Structural Refinement: Introduction of a Localized Molecular Orbital-Based Embedding for Accurate X-ray Determinations of Hydrogen Atom Positions. *J. Phys. Chem. Lett.*, **12**, 463-471 (2021). DOI: 10.1021/acs.jpclett.0c03421.
46. S. Grimme; S. Ehrlich; L. Goerigk. Effect of the damping function in dispersion corrected density functional theory. *J. Comput. Chem.*, **32**, 1456-1465 (2011). DOI: 10.1002/jcc.21759.
47. P. J. Stephens; F. J. Devlin; C. F. Chabalowski; M. J. Frisch. Ab Initio Calculation of Vibrational Absorption and Circular Dichroism Spectra Using Density Functional Force Fields. *J. Phys. Chem.*, **98**, 11623-11627 (1994). DOI: 10.1021/j100096a001.
48. J.-D. Chai; M. Head-Gordon. Long-range corrected hybrid density functionals with damped atom-atom dispersion corrections. *Phys. Chem. Chem. Phys.*, **10**, 6615-6620 (2008). DOI: 10.1039/b810189b.
49. J. P. Perdew; K. Burke; M. Ernzerhof. Generalized Gradient Approximation Made Simple. *Phys. Rev. Lett.*, **77**, 3865-3868 (1996).
50. J. Tao; J. P. Perdew; V. N. Staroverov; G. E. Scuseria. Climbing the Density Functional Ladder: Nonempirical Meta--Generalized Gradient Approximation Designed for Molecules and Solids. *Phys. Rev. Lett.*, **91**, 146401 (2003). DOI: 10.1103/PhysRevLett.91.146401.
51. S. Grimme. Semiempirical hybrid density functional with perturbative second-order correlation. *J. Chem. Phys.*, **124**, 034108 (2006). DOI: 10.1063/1.2148954.
52. F. Jensen. *Introduction to Computational Chemistry*. 3rd ed.; John Wiley & Sons: West Sussex (2017).
53. R. Krishnan; J. S. Binkley; R. Seeger; J. A. Pople. Self-consistent molecular orbital methods. XX. A basis set for correlated wave functions. *J. Chem. Phys.*, **72**, 650-654 (1980).
54. A. Schäfer; C. Huber; R. Ahlrichs. Fully optimized contracted Gaussian basis sets of triple zeta valence quality for atoms Li to Kr. *J. Chem. Phys.*, **100**, 5829-5835 (1994). DOI: 10.1063/1.467146.
55. P. C. Hariharan; J. A. Pople. The influence of polarization functions on molecular orbital hydrogenation energies. *Theor. Chem. Acc.*, **28**, 213-222 (1973).
56. F. Weigend; R. Ahlrichs. Balanced basis sets of split valence, triple zeta valence and quadruple zeta valence quality for H to Rn: Design and assessment of accuracy. *Phys. Chem. Chem. Phys.*, **7**, 3297-3305 (2005). DOI: 10.1039/b508541a.
57. J. G. Brandenburg; C. Bannwarth; A. Hansen; S. Grimme. B97-3c: A revised low-cost variant of the B97-D density functional method. *J. Chem. Phys.*, **148**, 064104 (2018). DOI: 10.1063/1.5012601.
58. S. Grimme; A. Hansen; S. Ehlert; J.-M. Mewes. r2SCAN-3c: A "Swiss army knife" composite electronic-structure method. *J. Chem. Phys.*, **154**, 064103 (2021). DOI: 10.1063/5.0040021.
59. F. Weigend. A fully direct RI-HF algorithm: Implementation, optimised auxiliary basis sets, demonstration of accuracy and efficiency. *Phys. Chem. Chem. Phys.*, **4**, 4285-4291 (2002). DOI: 10.1039/b204199p.
60. C. Bannwarth; S. Ehlert; S. Grimme. GFN2-xTB—An Accurate and Broadly Parametrized Self-Consistent Tight-Binding Quantum Chemical Method with Multipole Electrostatics and Density-Dependent Dispersion Contributions. *J. Chem. Theory Comput.*, **15**, 1652-1671 (2019). DOI: 10.1021/acs.jctc.8b01176.
61. S. Grimme; C. Bannwarth; P. Shushkov. A Robust and Accurate Tight-Binding Quantum Chemical Method for Structures, Vibrational Frequencies, and Noncovalent Interactions of Large Molecular Systems Parametrized for All spd-Block Elements (Z = 1–86). *J. Chem. Theory Comput.*, **13**, 1989-2009

(2017). DOI: 10.1021/acs.jctc.7b00118.
62. Stefan Grimme, et al., xtb program: https://github.com/grimme-lab/xtb/ (accessed on Nov 12, 2021).
63. A. D. Becke; K. E. Edgecombe. A Simple Measure of Electron Localization in Atomic and Molecular Systems. *J. Chem. Phys.*, **92**, 5397-5403 (1990). DOI: 10.1063/1.458517.
64. P. Fuentealba; E. Chamorro; J. C. Santos. Understanding and using the electron localization function. In *Theoretical Aspects of Chemical Reactivity*, A. Toro-Labbé, Ed. Elsevier B.V.: Amsterdam (2007); pp 57-85.
65. T. Lu; F. Chen. Meaning and Functional Form of the Electron Localization Function. *Acta Phys. -Chim. Sin.*, **27**, 2786-2792 (2011). DOI: 10.3866/PKU.WHXB20112786.
66. C. Lefebvre; G. Rubez; H. Khartabil; J.-C. Boisson; J. Contreras-García; E. Hénon. Accurately extracting the signature of intermolecular interactions present in the NCI plot of the reduced density gradient versus electron density. *Phys. Chem. Chem. Phys.*, **19**, 17928-17936 (2017). DOI: 10.1039/C7CP02110K.
67. M. Ponce-Vargas; C. Lefebvre; J.-C. Boisson; E. Hénon. Atomic Decomposition Scheme of Noncovalent Interactions Applied to Host–Guest Assemblies. *J. Chem. Inf. Model.*, **60**, 268-278 (2020). DOI: 10.1021/acs.jcim.9b01016.
68. T. Lu; Q. Chen. Independent gradient model based on Hirshfeld partition (IGMH): A new method for visual study of interactions in chemical systems. *ChemRxiv* (2021). DOI: 10.26434/chemrxiv-2021-628vh.
69. Y. Segawa; M. Kuwayama; Y. Hijikata; M. Fushimi; T. Nishihara; J. Pirillo; J. Shirasaki; N. Kubota; K. Itami. Topological molecular nanocarbons: All-benzene catenane and trefoil knot. *Science*, **365**, 272-276 (2019). DOI: 10.1126/science.aav5021.
70. T. Lu; F. Chen. Atomic Dipole Moment Corrected Hirshfeld Population Method. *J. Theor. Comp. Chem.*, **11**, 163-183 (2012). DOI: 10.1142/S0219633612500113.
71. F. L. Hirshfeld. Bonded-Atom Fragments for Describing Molecular Charge Densities. *Theor. Chem. Acc.*, **44**, 129-138 (1977).
72. T. Lu; F. Chen. Bond Order Analysis Based on the Laplacian of Electron Density in Fuzzy Overlap Space. *J. Phys. Chem. A*, **117**, 3100-3108 (2013). DOI: 10.1021/jp4010345.
73. S. M. Bachrach. Planar rings in nano-Saturns and related complexes. *Chem. Commun.*, **55**, 3650-3653 (2019). DOI: 10.1039/C9CC01234F.
74. C. Lefebvre; H. Khartabil; J.-C. Boisson; J. Contreras-García; J.-P. Piquemal; E. Hénon. The Independent Gradient Model: A New Approach for Probing Strong and Weak Interactions in Molecules from Wave Function Calculations. *ChemPhysChem*, **19**, 724-735 (2018). DOI: 10.1002/cphc.201701325.
75. P. Wu; R. Chaudret; X. Hu; W. Yang. Noncovalent Interaction Analysis in Fluctuating Environments. *J. Chem. Theory Comput.*, **9**, 2226-2234 (2013). DOI: 10.1021/ct4001087.
76. B. Hess; C. Kutzner; D. van der Spoel; E. Lindahl. GROMACS 4: Algorithms for Highly Efficient, Load-Balanced, and Scalable Molecular Simulation. *J. Chem. Theory Comput.*, **4**, 435-447 (2008). DOI: 10.1021/ct700301q.
77. J. Wang; R. M. Wolf; J. W. Caldwell; P. A. Kollman; D. A. Case. Development and testing of a general amber force field. *J. Comput. Chem.*, **25**, 1157-1174 (2004). DOI: 10.1002/jcc.20035.
78. T. Lu. Multiwfn Manual, version 3.8, Section 3.23.9, available at http://sobereva.com/multiwfn (accessed on Nov 29, 2021).
79. T. Lu; F. Chen. Revealing the nature of intermolecular interaction and configurational preference of the nonpolar molecular dimers (H2)2, (N2)2, and (H2)(N2). *J. Mol. Model.*, **19**, 5387-5395 (2013).

DOI: 10.1007/s00894-013-2034-2.
80. T. Lu; Q. Chen. van der Waals potential: an important complement to molecular electrostatic potential in studying intermolecular interactions. *J. Mol. Model.*, **26**, 315 (2020). DOI: 10.1007/s00894-020-04577-0.
81. Z. Wang; Y. Liu; B. Zheng; F. Zhou; Y. Jiao; Y. Liu; X. Ding; T. Lu. A theoretical investigation on Cu/Ag/Au bonding in XH2P···MY(X = H, CH3, F, CN, NO2; M = Cu, Ag, Au; Y = F, Cl, Br, I) complexes. *J. Chem. Phys.*, **148**, 194106 (2018). DOI: 10.1063/1.5027605.
82. M. P. Mitoraj; A. Michalak; T. Ziegler. A Combined Charge and Energy Decomposition Scheme for Bond Analysis. *J. Chem. Theory Comput.*, **5**, 962-975 (2009). DOI: 10.1021/ct800503d.
83. T. Lu; Z. Liu; Q. Chen. Comment on “18 and 12 – Member carbon rings (cyclo[n]carbons) – A density functional study”. *Mat. Sci. Eng. B*, **273**, 115425 (2021). DOI: 10.1016/j.mseb.2021.115425.
84. M. A. Spackman; D. Jayatilaka. Hirshfeld surface analysis. *CrystEngComm*, **11**, 19-32 (2009). DOI: 10.1039/B818330A.
85. T. Lu; Q. Chen. mwfn: A Strict, Concise and Extensible Format for Electronic Wavefunction Storage and Exchange. *ChemRxiv* (2020). DOI: 10.26434/chemrxiv.11872524.
86. T. D. Kühne; M. Iannuzzi; M. Del Ben; V. V. Rybkin; P. Seewald; F. Stein; T. Laino; R. Z. Khaliullin; O. Schütt; F. Schiffmann; D. Golze; J. Wilhelm; S. Chulkov; M. H. Bani-Hashemian; V. Weber; U. Borštnik; M. Taillefumier; A. S. Jakobovits; A. Lazzaro; H. Pabst; T. Müller; R. Schade; M. Guidon; S. Andermatt; N. Holmberg; G. K. Schenter; A. Hehn; A. Bussy; F. Belleflamme; G. Tabacchi; A. Glöß; M. Lass; I. Bethune; C. J. Mundy; C. Plessl; M. Watkins; J. VandeVondele; M. Krack; J. Hutter. CP2K: An electronic structure and molecular dynamics software package - Quickstep: Efficient and accurate electronic structure calculations. *J. Chem. Phys.*, **152**, 194103 (2020). DOI: 10.1063/5.0007045.